Turbulent boundary layer noise: direct radiation at Mach number 0.5

XAVIER GLOERFELT[1] AND JULIEN BERLAND[1]†

[1]DynFluid Laboratory, Arts et Metiers ParisTech, 151 bd de l'Hopital, 75013 Paris, France

(Received ?? and in revised form ??)

Boundary layers constitute a fundamental source of aerodynamic noise. A turbulent boundary layer over a plane wall can provide an indirect contribution to the noise by exciting the structure, and a direct noise contribution. The latter part can play a significant role even if its intensity is very low, explaining why it is hardly measured unambiguously. In the present study, the aerodynamic noise generated by a spatially developing turbulent boundary layer is computed directly by solving the compressible Navier-Stokes equations. This numerical experiment aims at giving some insight into the noise radiation characteristics. The acoustic wavefronts have a large wavelength and are oriented in the direction opposite to the flow. Their amplitude is only 0.7% of the aerodynamic pressure for a flat-plate flow at Mach 0.5. The particular directivity is mainly explained by convection effects by the mean flow, giving an indication about the compactness of the sources. These vortical events correspond to low-frequencies, and have thus a large life time. They cannot be directly associated with the main structures populating the boundary layer such as hairpin or horseshoe vortices. The analysis of the wall pressure can provide a picture of the flow in the frequency-wavenumber space. The main features of wall pressure beneath a turbulent boundary layer as described in the literature are well reproduced. The acoustic domain, corresponding to supersonic wavenumbers, is detectable but can

† Present address: EDF R&D, MFEE, I84, 6 Quai Watier, 78400 Chatou, France.

hardly be separated from the convective ridge at this relatively high speed. This is also due to the low frequencies of sound emission as noted previously.

Key Words: aeroacoustics; wall turbulence

---

1. Introduction

1.1. *Flow noise*

Aerodynamic noise from a turbulent boundary layer (TBL), also known as flow noise, is a fundamental topic in flow-induced noise. Its contribution to internal noise in terrestrial or aeronautic vehicles is increasing. With the recent progresses in reducing the other sources, such as road or motor noises for a car, or jet and fan noises for a plane, cabin noise due to the TBL has indeed become a matter of concern for manufacturers, in order to improve the comfort of passengers during cruising trip. Sound waves transmitted inside the interior of the vehicle come from two contributions: the *direct transfer* of the acoustic radiation, *i.e.* the self-noise generated by wall turbulence, and the *indirect transfer* by the wall pressure fluctuations which can excite the vibrational modes of the structure. The first one has a low efficiency but a transfer function close to one, whereas the second is more energetic but the transfer function becomes very weak at high wavenumbers, so that the direct contribution is not necessarily negligible with respect to the indirect vibroacoustic contribution. A quantitative evaluation of the contribution of the acoustic part to the internal noise is however still lacking.

Our knowledge of the noise directly radiated by a TBL relies almost exclusively on the acoustic analogy of Lighthill (1952) (see the reviews by Blake (1986*a*) and Dowling (1992)). A major contribution is given by Powell (1960), who showed that the surface

integrals of the formulation of Curle (1955) yield essentially quadripolar sources when an infinite plane is present. The principal implication of his so-called *reflection theorem* is that TBL noise sources are rather inefficient. The acoustic intensity follows a U^8 law as free turbulence whereas a compact rigid surface would yield a U^6 law. This inefficiency is thus particularly severe for low-speed flows. The tangential wall shear stresses are reinforced by the reflection, and can then constitute the principal sources, even if viscous motions are poor radiators notably at high Reynolds numbers (Haj-Hariri & Akylas (1985)). The weak levels of direct acoustic emissions also explain why few experiments are available so far, and can hardly provide clarifications on TBL sources. The first attempt consisted in placing hydrophones inside the TBL developing on the walls of a water tunnel (Skudrzyk & Haddle (1960)). The interpretation of the experimental results is however ill-posed because the transducers always introduce averaging effects, and a clear separation between pseudo-sound and radiated sound is impractical without an a priori knowledge about the turbulence inducing the pseudo-sound. Even if some tendencies are depicted such as the increased noise due to surface roughness, a quantitative measurement is also marred by the noisy environment, such as the machinery. Buoyant bodies were designed to cope with that (Haddle & Skudrzyk (1969); Sevik (1986)). The evaluation of flow noise from boundary layers of buoyancy-propelled vehicles is however hindered by other sources that can be more efficient, such as flow separations, or transition to turbulence. Measurements by Haddle & Skudrzyk (1969) seem to be dominated by radiations from the aft section, whereas experiments of Sevik (1986) are presumably contaminated by an exterior source since the results for smooth and rough walls yield the same estimate. Barker (1973) has measured the noise emissions from an open cylinder rotating in water, its generatrix in the form of a single-coil helix. A significant fraction of the sound was generated by the interaction of turbulence with the edge of the helix,

so that the sound from the TBL can be masked by this source. To provide a convincing separation between sound and pseudo-sound, Greshilov & Mironov (1983) removed the sensors from the working section of the hydrodynamic duct into an expanded diffuser. It is then necessary to separate the wall turbulence self-noise from the acoustic resonance modes of the diffuser, and the evaluation of the strength of the radiated noise is not far from ambiguity. A scatter of more than 40 dB between the different studies was noted.

Several theoretical studies have been carried out with the aim of predicting some features of the pressure field radiated by a plane TBL. Lighthill's theory and its extensions (Lighthill (1952); Curle (1955)) have then been extensively used in the study of the noise generated by TBL. Landahl (1975) for instance developed a two-scale model for the turbulent velocity and pressure fields in order to estimate the noise radiated by a the flow over a solid surface. Tam (1975) calculated the intensity, the directivity and the spectrum of the sound field produced by a TBL based on an empirical model for the pressure cross-correlation function. In a similar manner, the noise generated by specific features of the TBL has been investigated. In particular, Lauchle (1980) considered sound wave production during the boundary-layer transition. In an attempt to shed a new light on sound sources of TBL, Hardin (1991) analysed the noise generated by various vortical phenomena such as the formation of horseshoe vortices and the emergence of viscous sublayer bursts. The works reported above use an empirical expression or an assumed shape for the Fourier transform of the pressure cross-correlation function. To cope with the uncertainties associated with the choice of a cross-correlation model, the analogy of Lighthill (1952) has also been applied to aerodynamic data issued from numerical simulations. Hu *et al.* (2002, 2003, 2006*a*) focused on noise generated by turbulent channel flows. They applied Lighthill's acoustic analogy to incompressible Direct Numerical Simulation (DNS) data in order to obtain an expression for the power spectrum of the

far-field pressure fluctuations. Wang *et al.* (1996) evaluated the far-field sound of an unstable wavepacket over a solid surface, the features of the transition being provided by solving the incompressible Navier-Stokes equations. Yang & Wang (2009) have recently applied the same numerical strategy, based on an incompressible DNS followed by an acoustic analogy, to investigate how the aerodynamic noise is enhanced by surface roughness (Howe (1991)).

1.2. *Wall pressure*

Since the pressure is a non-localised variable, the wall pressure provides a fingerprint of the TBL structures. When the wall surface is locally plane, the temporal and spatial characteristics of the wall pressure can be expressed in terms of wavenumber-frequency spectrum $\Phi_{pp}(\mathbf{k},\omega)$. The shape of this spectrum is illustrated schematically in figure 1 for a fixed frequency ω satisfying $\omega\delta/U_\infty \gg 1$, where U_∞ is the freestream velocity and δ the boundary layer thickness. The strongest fluctuations occur at wavenumbers within the convective ridge centered on $k_1 = \omega/U_c$, $k_3 = 0$, where U_c is a turbulent eddy convection velocity. However the strongest coupling of wall motions and the flow is usually attributed to smaller wavenumbers, the subconvective region. The spectral levels are 30 to 60 dB below that of the convective peak. The region $|\mathbf{k}| < \kappa_0$, where $\kappa_0 = \omega/c_0$ is the acoustic wavenumber, is called the acoustic domain, and is more particularly the subject of the present study. The pressure fluctuations beneath a TBL have been the subject of numerous experimental and theoretical studies by Willmarth & Woolridge (1962), Bull (1967), Blake (1970), Wills (1970), Schewe (1983), Farabee & Casarella (1991), Panton & Robert (1994), Gravante *et al.* (1998), Arguillat *et al.* (2010), Ehrenfried & Koop (2008) among others (see the reviews by Willmarth (1975), or Blake (1986*a*)). With the development of supercomputers, the numerical simulation constitutes a new efficient approach. The wall-pressure field generated by incompressible direct numerical simulations (DNS)

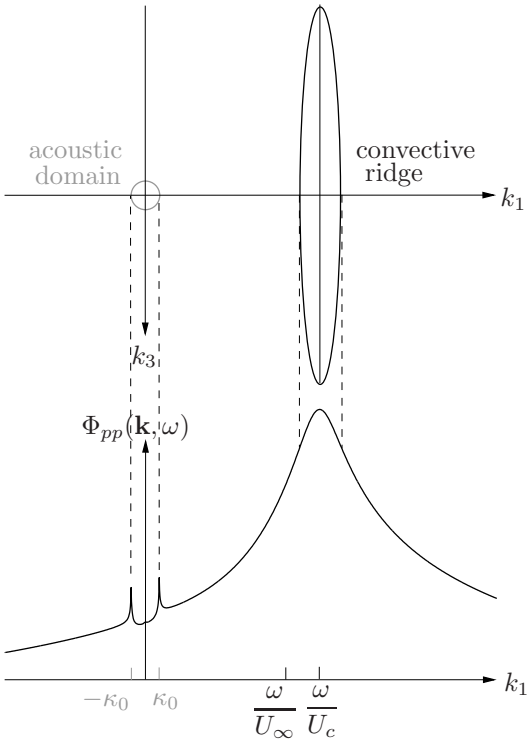

FIGURE 1. Wavenumber-frequency spectrum $\Phi_{pp}(\mathbf{k},\omega)$ for a frequency $\omega\delta^*/U_\infty$=500, where M_∞=0.1 and δ=2 cm. The model of Chase (1987) is used for illustration: $\Phi_{pp}(\mathbf{k},\omega) = \frac{\rho_0^2 u_\tau^3 \delta^3}{[(k_+\delta)^2+1/b^2]^{\frac{5}{2}}} \left[\frac{C_M (k_1\delta)^2 k^2}{|k^2-\kappa_0^2|+\epsilon^2\kappa_0^2} + C_T(k\delta)^2 \times \mathcal{F} \right]$ with $k_+^2 = (\omega - U_c k_1)^2/(hu_\tau)^2 + k^2$, and $\mathcal{F} = \frac{(k_+\delta)^2+1/b^2}{(k\delta)^2+1/b^2} \left(c_1 + \frac{c_2|k^2-\kappa_0^2|}{k^2} + \frac{c_3 k^2}{|k^2-\kappa_0^2|+\epsilon^2\kappa_0^2} \right)$. We set C_M=0.1553, C_T=0.0047, b=0.75, h=3, c_1=2/3, c_2=0.005, c_3=1/6, and ϵ=0.2.

and large-eddy simulations (LES) of channel flow has been investigated in the past by Kim (1989), Choi & Moin (1990), Chang *et al.* (1999), Viazzo *et al.* (2001), or Hu *et al.* (2006*b*). Furthermore, simplified semi-empirical models of wall-pressure fluctuations have been proposed. The most popular are the model of Corcos (1963) and the model of Chase (1980, 1987). Blake (1986*a*), Bull (1996), Graham (1997), or Hwang *et al.* (2009) propose comparisons between the different semi-empirical models.

Since the low wavenumber region is of particular interest for the possible coincidence with the stuctural modes, numerous authors have investigated the shape of the spectrum in the low wavenumber limit, notably for the supersonic wavenumbers ($k < \kappa_0$). A good

discussion of this problem is provided by Ffowcs Williams (1965, 1982). The Kraichnan-Phillips theorem (Howe (1992)), named after the studies of Kraichnan (1956) and Phillips (1956), states that $\Phi_{pp}(\mathbf{k},\omega)$ must tend toward zero as k^2 for an incompressible flow (Bull (1996)). The experimental verification of this theoretical point is difficult because vanishing wavenumber are not resolved (one of the most resolved experiment in the low frequencies has been conducted by Farabee & Casarella (1991)). However, numerical simulations for low-Reynolds-number channel flows seem to yield a non-vanishing limit as $k \to 0$ (Hu *et al.* (2002, 2003)). Furthermore, a theoretical evaluation of the acoustic magnitude is difficult due to the singularity at the acoustic-wavenumber κ_0, arising from the expression of the Green function in the frequency-wavenumber space for a half-plane, $G(x_2|y_2,\mathbf{k},\omega) = -i\mathrm{e}^{-\gamma x_2}/\gamma$ where $\gamma(k) = \mathrm{sgn}(\kappa_0)|\kappa_0^2 - k^2|^{1/2}$ for $k < \kappa_0$, and $\gamma(k) = i|\kappa_0^2 - k^2|^{1/2}$ for $k > \kappa_0$. A comprehensive discussion of the behavior of the spectrum near the acoustic-wavenumber singularity is provided by Howe (1991). Three main phenomena can remove the singularity:

- the finite size of the domain (theoretical works suppose an infinite plane). This point is first studied by Bergeron (1974) or Ffowcs Williams (1982);
- the viscous effect (see the elegant model of Howe (1979*b*,*a*)). Howe (1979*b*) suggests that the viscous terms have only a dissipative role. The numerical studies of Wang *et al.* (1996), Shariff & Wang (2005), or Hu *et al.* (2002) indicate that the dipole wall shear-stress can be a true source of sound for low Mach numbers;
- the curvature of the surface (Meecham (1965); Howe (1991)). Meecham (1965) has shown that a local surface curvature can result in a dipole sound.

The main contribution seems to be due to the finite size effect, but this is still an open question.

1.3. *Scope of the study*

In spite of the numerous works already achieved in the field of TBL noise, a clear identification of sound sources remains elusive. An investigation approach relying on Direct Noise Calculation (DNC) might therefore be valuable. Such simulations indeed aim at obtaining both aerodynamic and acoustic fields within a same run. The method is particularly reliable since the compressible Navier-Stokes equations are directly solved and no additional modeling of the acoustic sources is required. Performing DNC however remains a challenging issue: the full range of length and amplitude scales associated with aerodynamic and acoustic fluctuations needs to be resolved and silent non-reflecting boundary conditions must be implemented, as briefly described in section II. These requirements are especially difficult to meet for turbulent boundary layers. Validations of the flowfield against published results are proposed in section III. The features of the acoustic field obtained by the Direct Noise Computation are discussed in section IV. The wall pressure, which is often directly related to the noise emissions, is analysed in the last section.

2. Numerical methods and flow parameters

2.1. *Governing equations*

The full three-dimensional compressible Navier-Stokes equations are solved in a conservative form in a Cartesian coordinate frame :

$$\begin{aligned} \frac{\partial \rho}{\partial t} + \frac{\partial (\rho u_j)}{\partial x_j} &= 0 \\ \frac{\partial (\rho u_i)}{\partial t} + \frac{\partial (\rho u_i u_j)}{\partial x_j} + \frac{\partial p}{\partial x_i} - \frac{\partial \tau_{ij}}{\partial x_j} &= 0 \\ \frac{\partial (\rho E)}{\partial t} + \frac{\partial ((\rho E + p) u_j)}{\partial x_j} - \frac{\partial (\tau_{ij} u_i)}{\partial x_j} + \frac{\partial q_j}{\partial x_j} &= 0 \end{aligned} \tag{2.1}$$

where ρ, p, u_i are the density, pressure, and velocity components in the i-th coordinate

direction (i= 1, 2, 3). For an ideal gas, the total energy per mass unit E is defined as :

$$E = p/[(\gamma - 1)\rho] + u_i^2/2, \quad \text{and} \quad p = r\rho T,$$

where T is the temperature, r the gas constant, and γ the ratio of specific heats. The viscous stress tensor τ_{ij} is modeled as a Newtonian fluid, $\tau_{ij} = 2\mu S_{ij} + \lambda S_{kk}\delta_{ij}$ with $\lambda = -2\mu/3$ according to Stokes' hypothesis. $S_{ij} = (u_{i,j} + u_{j,i})/2$ is the rate of strain tensor. The dynamic molecular viscosity μ is approximated with Sutherland's law:

$$\mu(T) = \mu_0 \left(\frac{T}{T_0}\right)^{\frac{3}{2}} \frac{T_0 + 110.4}{T + 110.4}$$

with T_0=273.15 K and μ_0=1.711$\times 10^5$ kg.m^{-1}.s^{-1}. The heat flux component q_j models thermal conduction in the j-direction with Fourier's law $q_j = -(\mu c_p/\mathrm{Pr})(\partial T/\partial x_j)$, where Pr=0.72 is the Prandtl number, and c_p is the specific heat at constant pressure.

2.2. *Space and time discretizations*

The convective terms of (2.1) are integrated in time using an explicit low-storage six-step Runge-Kutta scheme optimised in the wavenumber space by Bogey & Bailly (2004). Because of their slower time evolution, the viscous terms are only integrated in the last substep. The gradients are solved on a rectangular slowly nonuniform grid by using finite-differences on an eleven-point stencil optimised by Bogey & Bailly (2004) for the convective fluxes, and standard fourth-order finite differences for the viscous and heat fluxes. The non-uniformity in the mesh sizes is taken into account by a suitable 1-D coordinate transform. At the last substep, a selective filtering on an eleven-point stencil (Bogey & Bailly (2004)) is incorporated in each direction to eliminate grid-to-grid unresolved oscillations. It is applied with an amplitude of 0.2.

On the wall boundary, the no-slip conditions $u_i = 0$ are imposed, with $\partial p/\partial n = 0$ for the Eulerian part, where n is the direction normal to the solid surface. The finite-difference stencil for the convective terms is progressively reduced down to the second

order. At the wall, the temperature is calculated with the adiabatic condition, so that the density can be deduced using ideal gas law. The viscous stress terms are evaluated from the interior points by using fourth-order backward differences. At the upstream and upper boundaries of the computational domain, the radiation boundary conditions of Tam & Dong (1996), using a far-field solution of the sound waves, are applied. A large sponge zone (Bogey & Bailly (2002); Gloerfelt & Lafon (2008)) is furthermore added at the downstream end of the domain so that unhindered passage of aerodynamic perturbations is possible without the generation of spurious acoustic waves. A three-dimensional planar domain is considered with periodic boundary conditions in the spanwise direction.

2.3. *Simulation parameters*

The spatial development of a three-dimensional turbulent boundary layer is calculated by means of compressible Large Eddy Simulation (LES). The LES strategy, combining a finite-difference scheme with good spectral properties with the use of a selective filtering without an additional eddy-viscosity model, bears some similarities with some new trends of the LES approach. The explicit filtering provides a smooth defiltering by removing the fluctuations at wavenumbers greater than the finite-difference scheme resolvability. As demonstrated by Mathew *et al.* (2003), the effect of the Approximate Deconvolution Model (ADM) is globally similar to the convolution with an explicit filter. Moreover, the selective filtering induces a regularization similar to that used in the ADM procedure, even if the coefficient is taken constant. Since it does not affect the resolved scales, the exact value of the coefficient is not crucial (see Bogey & Bailly (2006)). Another advantage is the versatility of this LES strategy, since no additional effort is required, whereas more elaborate models can induce 20% to one order of additional cost.

A sketch of the computational domain and of the coordinate system is provided in figure 2: x_1 is the streamwise direction and the flow goes from left to right; the wall is

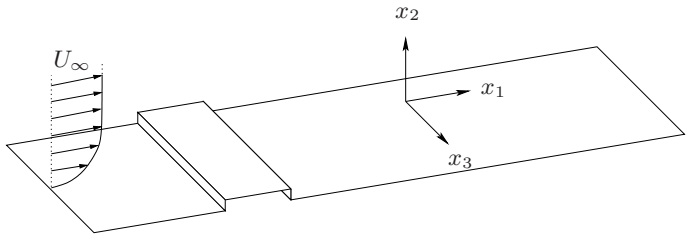

FIGURE 2. Sketch of the computational domain and of the coordinate system (figure not to scale). A small step lying in the spanwise direction is introduced downstream of the inlet boundary condition in order to ignite the transition to turbulence of the boundary layer flow.

	M_∞	p_∞ (Pa)	T_∞ (K)	ν_∞ (m^2/s)	δ_0 (m)	Re_θ^0
coarse grid	0.5	101 300	298.15	1.5×10^{-5}	2.5×10^{-4}	300
fine grid	0.5	101 300	298.15	1.5×10^{-5}	3.18×10^{-4}	480

TABLE 1. Flow configurations for the LES of a three-dimensional spatially developing turbulent boundary layer.

located in the plane $x_2 = 0$. Two simulations are conducted (hereafter referred to as coarse- and fine-grid LES) to check the sensitivity of the results on the spatial resolution.

2.3.1. *Inflow condition: triggering transition*

At the upstream frontier of the computational domain the boundary layer is assumed to be laminar. A third-order polynomial fit to the Blasius velocity profile is enforced at this location with an initial boundary layer thickness δ_0. The free-stream Mach number is taken to be $M_\infty = 0.5$. The pressure and density are set initially to uniform values p_∞ and $\rho_\infty = p_\infty/(rT_\infty)$. The initial Reynolds number Re_θ^0 based on the local momentum thickness θ of the laminar boundary layer are given in table 1 for the two simulations.

Turbulence seeding is achieved by introducing a small step slightly downstream of the inlet boundary condition. The step lies in the spanwise direction and is located between $x_1/\delta_0 = 11$ and $x_2/\delta_0 = 15$, and $0 \leqslant x_2/\delta_0 \leqslant 0.14$ for the coarse-grid LES, and between

	Δx_1^+	Δx_2^+	Δx_3^+	$\Delta t U_\infty/\delta_0$	N_{x_1}	N_{x_2}	N_{x_3}	$L_{x_1}/\delta_0^\dagger$	L_{x_2}/δ_0	L_{x_3}/δ_0	u_τ (m/s)
coarse grid	58	3	17.5	0.011	760	200	101	300	57	14	7.5
fine grid	37	0.98	14.7	0.0032	1372	300	131	287	400	12.2	7.38

TABLE 2. Grid parameters for the LES of a three-dimensional spatially developing turbulent boundary layer († without the sponge zone).

$x_1/\delta_0 = 5.7$ and $x_2/\delta_0 = 9$, and $0 \leqslant x_2/\delta_0 \leqslant 0.26$ for the fine-grid LES. This step has a large width-to-height aspect ratio and is hence expected to have few impact on the global mean flow while providing a discontinuity igniting the transition to turbulence. As explained in previous papers by Berland & Gloerfelt (2008) and Gloerfelt & Berland (2009), controlled laminar breakdown is not considered in the present study since the enforcement of aerodynamic perturbations at the inflow boundary, without generating spurious sound waves, remains a difficult task. The small step will induce some spurious noise, since a rough wall is known to generate higher noise levels than a smooth wall (Howe (1991)). Nevertheless, the trick used to ignite transition toward a fully turbulent state has the great advantage to be steady, and has been seen to produce considerably less spurious noise than other inflow conditions based on the introduction of unsteady perturbations (Gloerfelt & Le Garrec (2008); Berland & Gloerfelt (2008)), which is a crucial point to capture the direct radiation from the boundary layer turbulence.

2.3.2. *Grid design*

The mesh size is taken to be uniform in the spanwise direction. In a similar manner, the mesh in the streamwise direction is uniform but grid stretching, with a rate of 2%, is used in the sponge zone over the last 100 points. In the wall normal coordinate, the grid size is stretched using a geometric progression of 2% and 2.5% for the coarse- and fine-grid LES respectively. The resolution and domain size for each computation are given

in table 2. The friction velocity u_τ is calculated when the flow is fully turbulent. This reference velocity allows in particular to express simulation parameters in wall units, *e.g.* $\bar{u}^+ = \bar{u}/u_\tau$ or $x_i^+ = u_\tau x_i/\nu$. The values obtained by using the value at the middle of the computational domain are given in table 2. The total number of grid points is approximately 15 million for the coarse- and 54 million for the fine-grid LES. For this latter simulation, the transient stabilisation of the computation lasted 400 000 iterations and the statistics have been evaluated for the 600 000 following iterations. The overall cost of such a simulation is more than 5000 hours on a NEC-SX8 supercomputer.

3. Characteristics of the turbulent boundary layer

3.1. *Mean flow*

The mean flow provided by the present LES calculations is compared to reference data of Jimenez *et al.* (2010) obtained at $\mathrm{Re}_\theta = 1551$. The profile in the wall-normal direction of the mean streamwise velocity, $\overline{u}_1^+ = \overline{u}_1/u_\tau$, is presented in wall units in figure 3(a). In the viscous sublayer, the two LES predict fairly well the linear law. In the overlap region ($30 < y^+ < 200$), the DNS data of Jimenez *et al.* (2010), the log law and the present profiles perfectly collapse. Further away from the wall, for $y^+ > 200$, the classical wake defect is visible. A slight underprediction of the friction is noticeable on the coarse grid, which is often observed with LES-like resolution (Garnier *et al.* (2009)). The fine grid allows the prediction of the friction in very good agreement with the DNS. The evolutions of the shape factor along the streamwise direction are plotted in figure 3(b). They are compared to a momentum integral estimate (reported in Lund *et al.* (1998)) based on Coles' law. A fairly good agreement is observed for the decrease of the shape factor.

Figure 4 shows the vertical variations of the turbulent intensities near the end of the computational domain. Comparisons of these distributions with those of DNS references

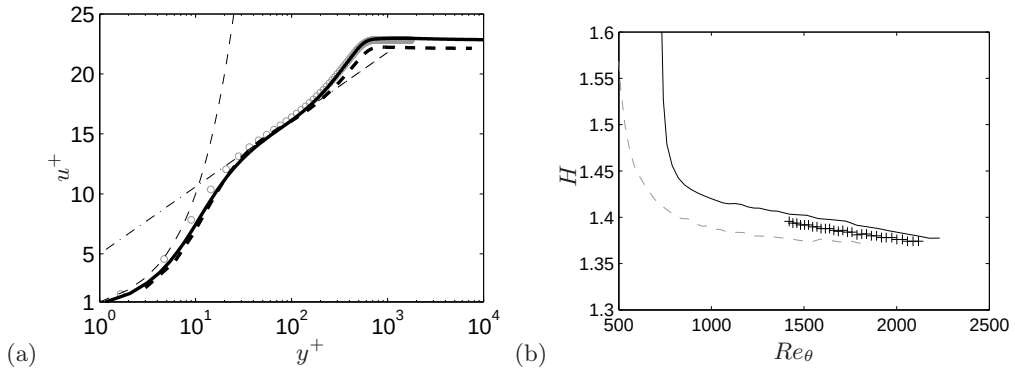

FIGURE 3. (a) Profiles of the mean longitudinal velocity in wall coordinates for the fine-grid LES at $x_1/\delta_{\rm ref}$=41.5 (Re$_\theta$=1551) (——), and for coarse-grid LES at $x_1/\delta_{\rm ref}$=62.3 (Re$_\theta$=1550) (– – –), compared with DNS of Jimenez *et al.* (2010) at Re$_\theta$=1551 (○). (b) Evolution of the shape factor H: (– – –) coarse-grid LES; (——) fine-grid LES; (+++) momentum integral estimate from Lund *et al.* (1998).

Spalart (1988) and Jimenez *et al.* (2010) indicate fairly good agreement for the fine meshgrid, whereas the levels are underestimated in the middle of the TBL with the coarse meshgrid. The tendency to underpredict the $u_{2_{\rm rms}}$ and $u_{3_{\rm rms}}$ is also common with LES resolution. The main features of a low-Reynolds-number turbulent boundary layer are satisfactorily reproduced for a range of Reynolds numbers based on the momentum thickness between 800 and 2400 on the fine grid.

3.2. *Instantaneous flow field*

Figure 5 shows instantaneous views of the norm of the vorticity for the fine-grid case. The onset of realistic turbulence is seen to occur between 5 and 10$\delta_{\rm ref}$, where $\delta_{\rm ref}$=1.13 mm is the boundary layer thickness at the middle of the computational domain. At this location, the displacement thickness is $\delta^*_{\rm ref} = 0.197$ mm. $\delta_{\rm ref}$ and $\delta^*_{\rm ref}$ are used as reference length scales throughout the paper. The total length of the domain in the longitudinal direction, required to resolve low wavenumbers, can be appreciated from figure 5. Furthermore, the

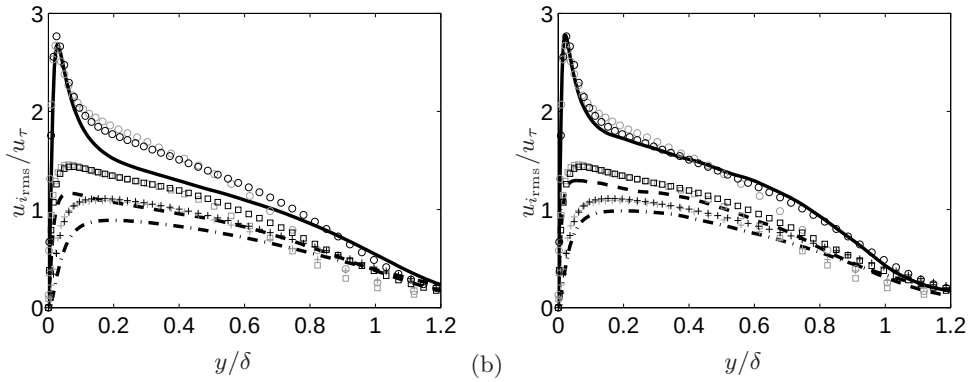

FIGURE 4. Turbulent intensities: $u_{1_{\rm rms}}/u_\tau$ (—— present LES; ○ Spalart; ○ Jimenez), $u_{2_{\rm rms}}/u_\tau$ (– · – · present LES; + Spalart; + Jimenez), $u_{3_{\rm rms}}/u_\tau$ (– – – present LES; □ Spalart; □ Jimenez). (a) coarse-grid LES results at $x_1/\delta_{\rm ref}$=79.1, and (b) fine-grid LES results at $x_1/\delta_{\rm ref}$=73.

characteristics of the flow structures are similar with previous DNS results by Spalart (1988), or with experimental smoke pictures of Head & Bandyopadhyay (1981).

4. Direct acoustic radiation

The acoustic pressure is obtained directly from DNC. In this section, the features of noise radiation outside the TBL, namely its frequency content, its directivity and the noise levels are analysed. The analysis is conducted for the fine-grid LES since similar conclusions are obtained with the coarser grid.

4.1. *Frequency content*

Overviews of the radiated field are given in figure 6, where the pressure fluctuation p' is plotted as a colormap. Acoustic wavefronts observed in the near-field are mainly oriented in the direction opposite to the flow, and have relatively large wavelengthes. Two instants are shown to get insight into the time variation of the acoustic field (see also the supplementary movie 1).

The time evolution of the pressure perturbation measured in the near-field is plotted

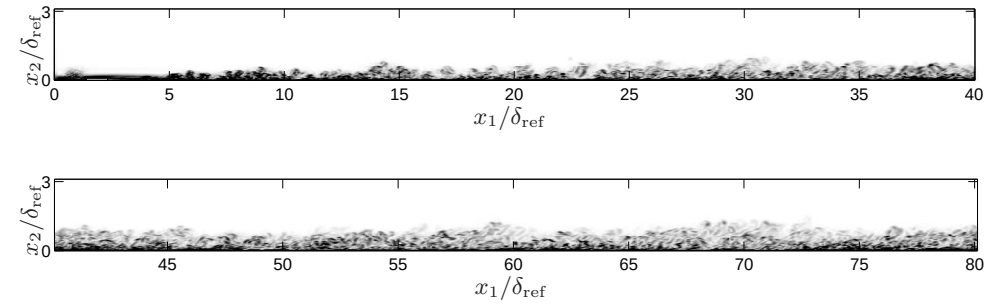

(a)

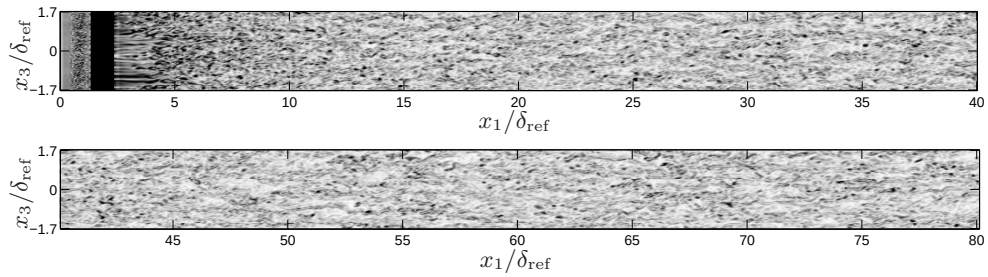

(b)

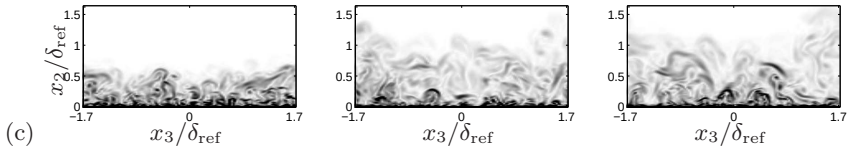

(c)

FIGURE 5. Instantaneous snapshots of the norm of the vorticity: (a) sideview in the median plane $x_3 = 0$ (the longitudinal length has been divided in two parts); (b) topview at $x_2 = 0.054\delta_{\rm ref}$; (c) 3 crossviews at $x_1/\delta_{\rm ref}$=19.8, 59.7, 72.9.

in figure 7 as a function of the non dimensional time $tU_\infty/\delta^*_{\rm ref}$. The peak amplitude of the signal is about 5 Pa at a distance $x_2/\delta^*_{\rm ref} \simeq 10$. Low-frequency events are noticeable, for instance with an approximate duration $TU_\infty/\delta^*_{\rm ref}$=100, marked by arrows in figure 7. The corresponding frequency $\omega\delta^*_{\rm ref}/U_\infty \simeq 0.06$ corresponds to the peak of the premultiplied spectra in figure 8(a). By plotting the spectrum in this way, the visual area under the curve in this semilogarithmic plot is proportional to the value of $\overline{p^2}$. The spectra are evaluated with Welch method for 19 500 samples recorded every $30\Delta t$, giving a sampling

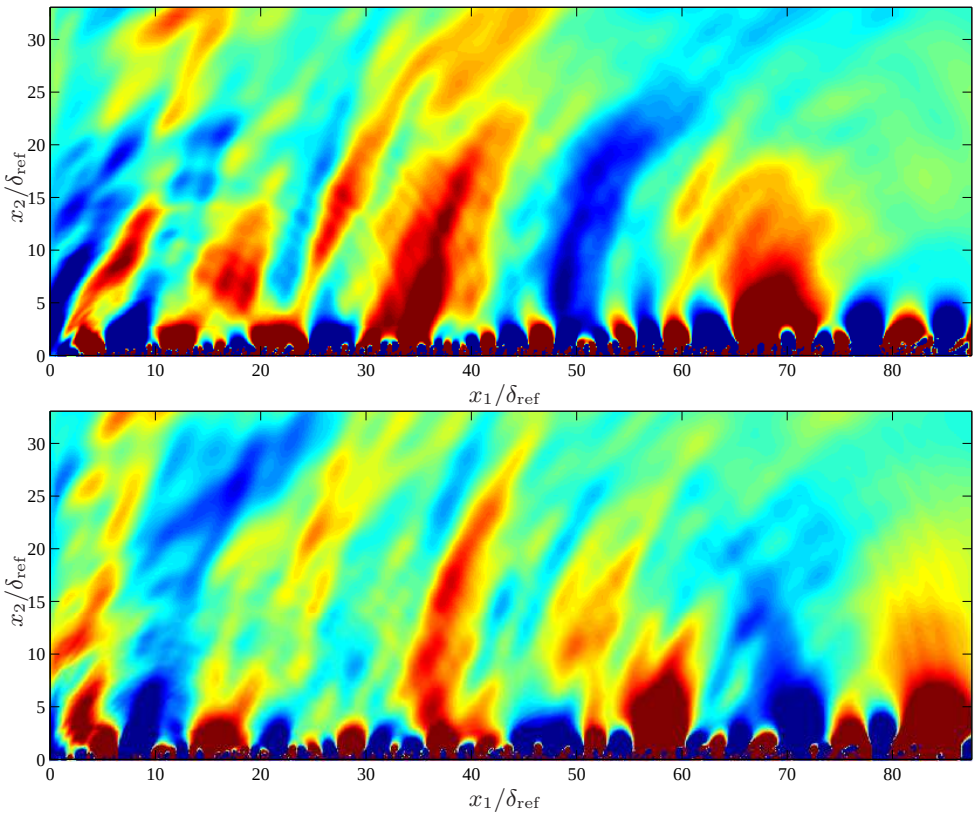

FIGURE 6. Instantaneous snapshots of the pressure fluctuations p' in the median plane (levels ± 5 Pa) at two instants for the fine-grid LES: $tU_\infty/\delta^*_{\rm ref}$=380.7 (top), and 1142.1 (bottom).

frequency of 5.77×10^6 Hz. The signal is splitted in 10 segments with 50% overlap, and a Hann window is applied to each segment. The broadband spectra in figure 8(b) show a good collapse at the different streamwise locations. Distinct high-frequency peaks are visible with Strouhal numbers 0.6, 1.24 (first harmonic) and 1.8 (second harmonic). It will be shown that these high-frequency components originate mainly from the small step used at the inlet to ignite turbulent transition.

In order to characterise more distinctly the features of the acoustic field at the different frequencies, the pressure in the median plane x_3=0 was stored (10 000 samples every $30\Delta t$), and band-pass filtered. Three particular reduced frequencies are selected, namely a low-frequency $\omega\delta^*_{\rm ref}/U_\infty$=0.033, a medium frequency $\omega\delta^*_{\rm ref}/U_\infty$=0.20, and a

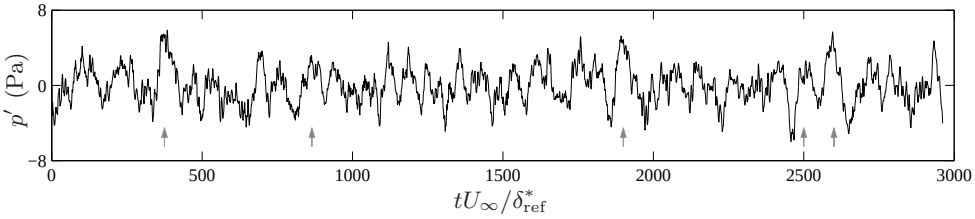

FIGURE 7. Time evolution of the pressure fluctuations as a function of non dimensional time $tU_\infty/\delta^*_{\rm ref}$ at $(x_1, x_2, x_3) = (46.4\delta_{\rm ref}, 9.6\delta_{\rm ref}, 0)$. The time origin corresponds to the end of the transient period, where statistics begin to be computed. The full length of the signal used for spectral analysis is shown.

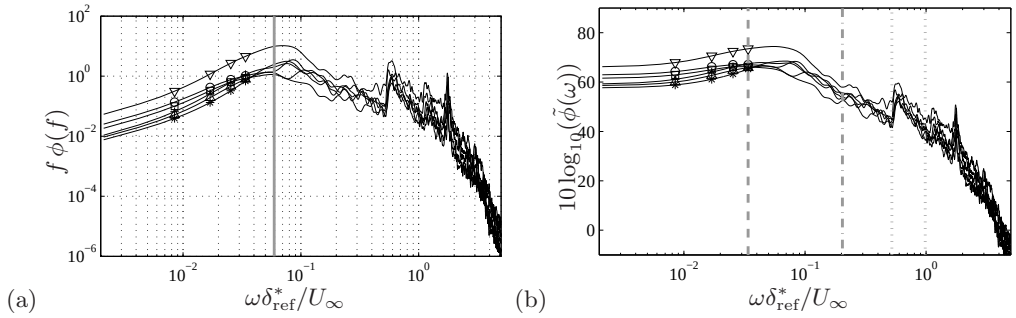

FIGURE 8. Premultiplied spectra $f\,\phi(f)$ (a), and normalized power spectral density $\tilde{\phi}(\omega) = \phi(\omega)U_\infty/(\rho^2 u_\tau^4 \mathrm{M}^2 \delta^{*3})$ (b) in the acoustic field at $x_2/\delta_{\rm ref} = 9.6$, and for various streamwise locations: $x_1/\delta_{\rm ref} = 6.6$ ($\triangledown$), 19.8 ($\circ$), 33.1 ($*$), 46.4 ($+$), 59.7 ($\triangle$), 72.9 ($\square$). On the left, the vertical solid line marks the peak $\omega\delta^*_{\rm ref}/U_\infty$=0.06. On the right, the dashed line indicates $\omega\delta^*_{\rm ref}/U_\infty$=0.033, the dash-dotted $\omega\delta^*_{\rm ref}/U_\infty$=0.20, and the two dotted lines at $\omega\delta^*_{\rm ref}/U_\infty$=0.52 and 0.99 define the high-frequency band, used in the Fourier analysis of §4.2.

high-frequency band, located around the first high-frequency peak. They are indicated by vertical lines in the spectra of figure 8(b). A forward-backward filtering (Gustafsson (1996)) is applied using second-order band-pass Butterworth filters. Colormaps of the filtered pressure are shown in figure 9 (see also supplementary movies 2-4). The resulting pressure field for the lowest frequency includes few wavelengthes, so that it is difficult to identify precisely the source locations. It is however clear in figure 9(a) that the source neither originates from the step or the outlet boundary. The plot for the intermediate

frequency in figure 9(b) also indicates significant time-to-time variations. The wavelength c_0/f=10.8$\delta_{\rm ref}$ now allows the identification of several sources, clearly originating from the TBL. The pressure field represents then an interference pattern. All the low-frequency components are characterised by a marked directivity in the direction opposite to the flow, to be discussed in the next section.

Finally, the pressure fields in figure 9(c), band-pass filtered around the first high-frequency peak, which was attributed to the diffraction by the small step near the inlet, are a superposition of circular wavefronts emanating from the step and high-frequency waves oriented in the direction opposite to the flow all along the TBL. The pressure levels for this frequency band are much higher near the step, confirming that the high-frequency peaks are indeed associated with diffracted waves from the step. The directivity of this unwanted source is fortunately also preferentially in the upstream direction, so that that most of the noise from the supplementary source escapes through the inlet boundary. It is associated with a Kelvin-Helmholtz-like instability, since the wall-normal velocity profiles exhibit an inflectional point just after the step. For instance, in figure 10, the mean streamwise velocity $\overline{u}/U_\infty$ is reported for various streamwise positions after the step. A composite profile is fitted by combining a Blasius profile and a hyperbolic-tangent profile:

$$\bar{u} = u_{\rm BL} \times W(\eta) \quad \text{with} \quad \frac{u_{\rm BL}}{U_\infty} = \begin{cases} \eta(2-2\eta^2+\eta^3) & \text{if} \quad \eta < 1 \\ 1 & \text{if} \quad \eta \geqslant 1 \end{cases}, \qquad (4.1)$$
$$W(\eta) = \tfrac{1}{2}\left\{1 + \tanh\left[\tfrac{a(\eta-b)}{(1-2b)\eta+b}\right] / \tanh(a)\right\}$$

where $\eta = y/\delta_1$, and the parameters are $\delta_1 \simeq 4\times10^{-4}$ m, a=3.3, b=0.25δ_1. A local viscous linear stability analysis is conducted for the composite profile. Details of the numerical method are specified in Robinet *et al.* (2001). The frequency of the most unstable wave is $\omega\delta^*_{\rm ref}/U_\infty$=0.603 in very good agreement with the value $\omega\delta^*_{\rm ref}/U_\infty \simeq$0.6 deduced from

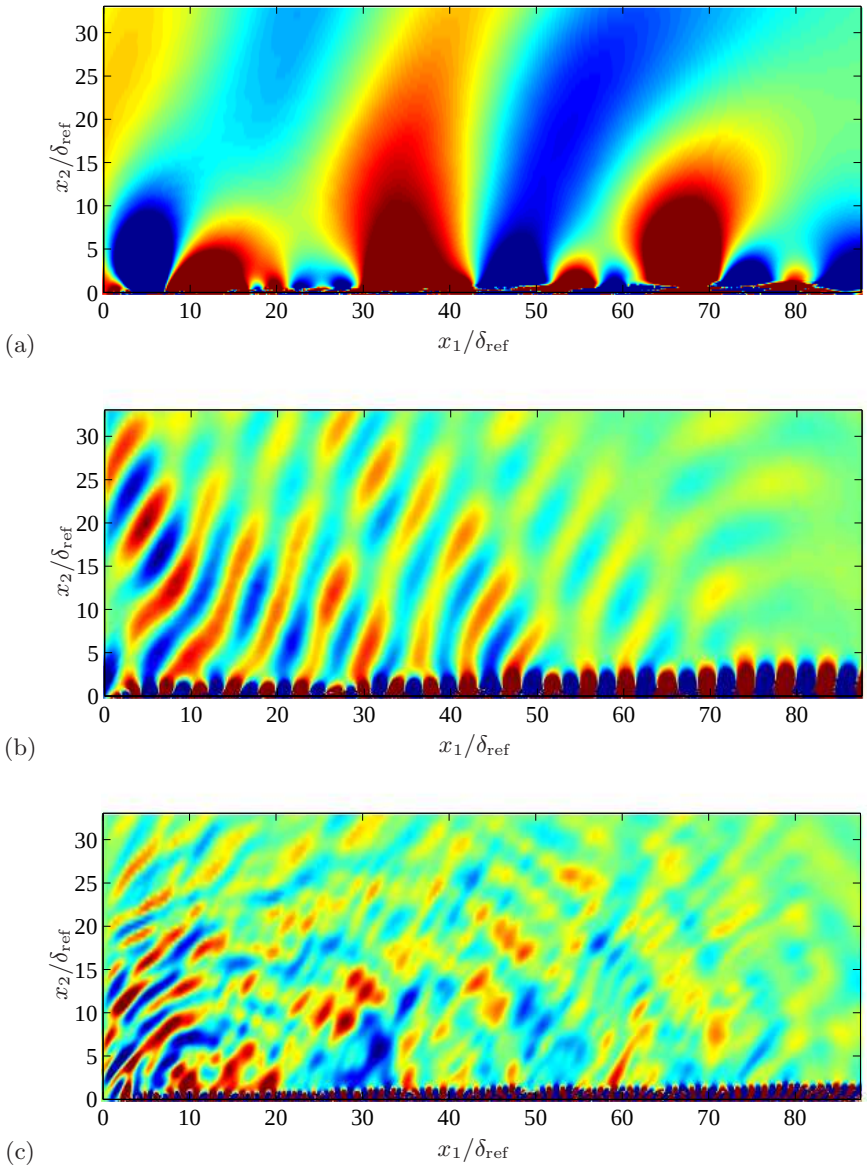

FIGURE 9. Band-pass filtered pressure in the median plane at $tU_\infty/\delta^*_{\rm ref}$=380.7: (a) around $\omega\delta^*_{\rm ref}/U_\infty$=0.033 (range ±0.5 Pa), (b) around $\omega\delta^*_{\rm ref}/U_\infty$=0.20 (range ±0.25 Pa), and (c) for the frequency band $\omega\delta^*_{\rm ref}/U_\infty \in [0.52; 0.99]$ (range ±1 Pa).

DNC spectra of figure 8. The trick used to ignite the turbulent inflow will thus pollute all the high-frequency part of the spectra. This spurious source however does not affect

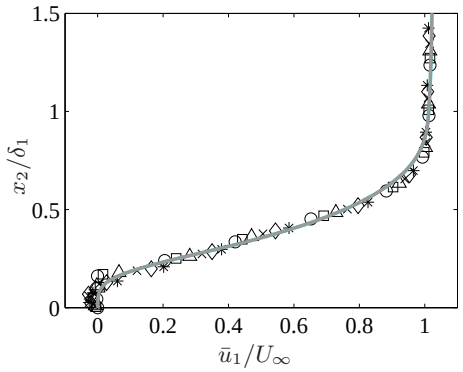

FIGURE 10. Profiles in the wall-normal direction of the mean streamwise velocity $\overline{u}/U_\infty$ as a function of y/δ_1 ($\delta_1 = \delta_0+$ step height), for successive streamwise locations just downstream the small step: x/δ_1= 7.28 (○), 7.65 (□), 8.02 (△), 8.40 (×), 8.77 (◇), 9.14 (*). The composite profile (4.1) is superimposed (——).

the low-frequency range of interest, and appears to be a better compromise than having used synthetic turbulence or recycling methods.

4.2. *Directivity of noise radiation*

The particular directivity in the direction opposite to the main stream, observed at all frequencies, can mainly be explained by propagation effects. In the present study, noise radiation is dominated by low frequencies. The case of a point source at the highest low frequency selected in the Fourier analysis, $\omega\delta^*_{\rm ref}/U_\infty$=0.2, is investigated in the appendix A. The main propagation effect is the convection due to the high-speed stream at M=0.5. The Doppler effect for a compact source decreases the wavelength upstream of the source, and conversely increases it downstream. This is accompanied by a rise of pressure levels upstream. The wavefront have consequently a very large apparent wavelength and low levels downstream of the source, explaining essentially the observed directivity. The concentration of sound power in a lobe oriented in the upstream direction, in agreement with the theory of compact sources, can help to conclude that the source inside the TBL are compact, and thus correspond to localised turbulent event. The convection effect is

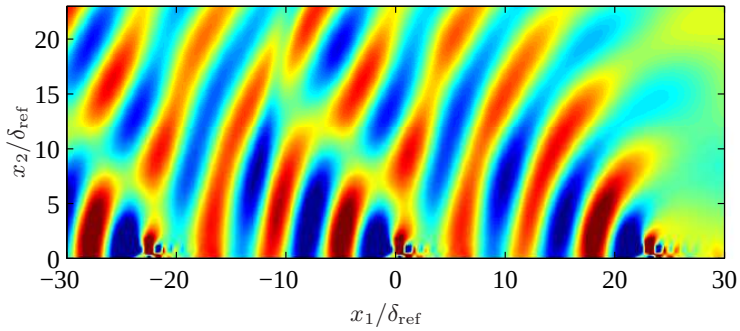

FIGURE 11. Pressure field obtained by placing three horizontal longitudinal quadrupoles inside a turbulent boundary-layer velocity profile. The source frequency is $\omega\delta^*_{\rm ref}/U_\infty$=0.2, their height is $0.016\delta_{\rm ref}$.

reinforced for higher-order multipolar sources. For instance for horizontal dipole or longitudinal quadripole, expected to be the dominant sources in a Lighthill-Powell analogy (Gloerfelt (2010)), the reflections at the wall and the multipolar nature yield intense beam in the upstream direction (see figure 26(b) and (e) in appendix A). The more complicated pressure pattern observed in figure 6 is a result of the superposition of several sources for a continuum of low frequencies, and with important time-to-time variations. For instance in figure 11, placing three compact longitudinal quadripoles close to the wall inside a mean turbulent velocity profile for the reduced frequency $\omega\delta^*_{\rm ref}/U_\infty$=0.2 yields an interference pattern bearing strong similarities with the TBL sources filtered at this frequency in figure 9(b).

4.3. *Amplitude of sound radiation*

At low Mach numbers, several authors give a simple relation between the acoustic domain of the wavenumber-frequency spectrum $\Phi_{pp}(k_1, k_3, \omega)$ and the frequency spectrum of the radiated sound (Blake (1986*b*); Dowling (1992); Howe (1998)). For instance Howe (1998, p. 211-212) relates the wavenumber-frequency spectrum of the pressure radiated in the far-field Φ_r and the acoustic domain of the wall pressure Φ_w for $k < \kappa_0$ using the

stationary phase assumption:

$$\Phi_r(\mathbf{x},\omega) = \frac{2\mathcal{A}\kappa_0^2\cos^2\theta}{|\mathbf{x}|^2}\Phi_w(\kappa_0\mathbf{x}/|\mathbf{x}|,\omega) \tag{4.2}$$

where $\mathcal{A}$ represents the area of the wetted surface, and $\theta = \cos^{-1}(x_2/|\mathbf{x}|)$. Dowling (1992, p. 461) gives two empirical expressions for the wall-pressure spectrum in the acoustic domain. The first one is deduced from the modified Chase (1987) model, which is derived from considerations about the Lighthill theory:

$$\Phi_w(0,\omega) \simeq 9.1\times10^{-4}\frac{\rho_\infty^2 u_\tau^4 \mathrm{M}^2 {\delta^*}^3}{U_\infty}\left(\frac{\omega\delta^*}{U_\infty}\right)^{-1} \tag{4.3}$$

The other expression is provided by Sevik (1986), who fitted experimental points on a buoyant body for a frequency range $3 < \omega\delta^*/U_\infty < 30$:

$$\Phi_w(0,\omega) = 5.6\frac{\rho_\infty^2 u_\tau^4 \mathrm{M}^2 {\delta^*}^3}{U_\infty}\left(\frac{\omega\delta^*}{U_\infty}\right)^{-4.5} \tag{4.4}$$

The results obtained with equations (4.3), and (4.4), inserted in (4.2), taking $\theta = 0$ and $\mathcal{A} = 74.28\delta_{\mathrm{ref}} \times 3.45\delta_{\mathrm{ref}}$, are superimposed on the acoustic spectrum from the LES in figure 12. The results for the Sevik formula are generally considered to be a higher bound for the quadrupole noise from a turbulent boundary layer. The acoustic results that he used are indeed presumably contamined by a source of exterior noise since the results for smooth and rough surface are identical (which is contradictory). Moreover, the range of validity is rather for high frequencies $\omega\delta^*/U_\infty > 1$, and low Mach numbers. We can indeed see that that the sound levels are greatly overestimated, even if the exponent for the frequency dependence seems roughly correct in the intermediate range. The levels predicted by the modeling of the acoustic domain used in Chase's model are in better agreement, but the frequency dependence is less favorable. Note also that the location of the receiver point is not in the very far field as assumed in the stationary phase approximation. The reliability of the various models remains controversial even after

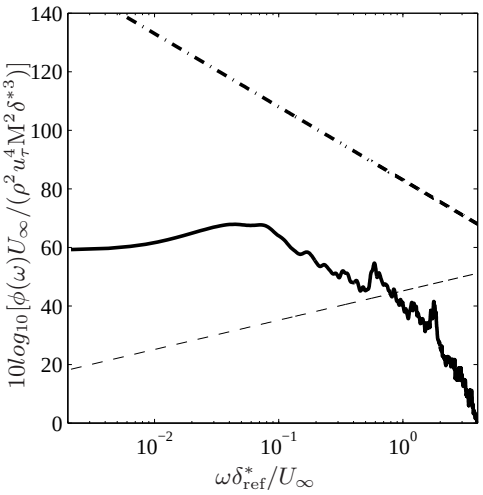

FIGURE 12. Comparisons of power spectral density of the pressure perturbations in the acoustic field with theoretical models: (——) Fine-grid LES at $x_1/\delta_{\rm ref} = 46.4$ and $x_2/\delta_{\rm ref} = 9.6$, (– – –) Chase's model Eq.(4.3), (— - — - —) Sevik's model Eq.(4.4).

several decades of investigation. The results from a DNC solver can thus help to revisit these models.

5. Analysis of wall-pressure fluctuations

Most of the models of flow noise rely on expressions of the wall pressure frequency-wavenumber spectrum. The investigations mainly concentrated either on flows at very low Mach numbers M$\ll$ 1 as in underwater applications, or in the context of ground vehicles. In the present study, a compressible turbulent boundary layer at M=0.5 is tackled, which can be relevant for cabin noise, generated at the fuselage of an airplane. The analysis of wall pressure fluctuations aims at characterizing the turbulent motions responsible for the noise emissions.

An analysis in the wavenumber-frequency domain yields a direct link between the acoustic radiation and the source fluctuations having supersonic wavenumber components, in the absence of any scatterer. It is therefore crucial to take care of the spectral

resolution, especially in the low wavenumber region. This is indeed strenuous to measure the low wavenumbers in the acoustic region, either because of the finite extent of the model or of the microphone array, or because of the contamination by the background noise of the wind tunnel facility. The question whether the spot possibly visible in the acoustic region, is coming from the boundary layer self-noise or the environment noise is still open. Two experimental works report a spot in the acoustic domain. Arguillat *et al.* (2010) (see also Arguillat (2006)) used 63 remote microphone probes along the diameter of a disk. The transducers line is turned, allowing to scan with discrete values a complete disk. They studied low-speed boundary layers typical of automotive applications. The wavenumber-frequency spectrum at 1000 Hz for a flat plate turbulent boundary layer at U_∞=40 m/s and δ^*=10.5 mm is consistent with the Corcos model concerning the convective ridge. The presence of an acoustic domain with a magnitude of 5% of the aerodynamic field is observable. Ehrenfried & Koop (2008) studied a high-speed flat plate boundary layer (M=0.83, $\delta^*\approx$4 mm). They obtained wavenumber-frequency spectra from a 48-sensor array with a beamforming method. The resolution is increased by the embedded DAMAS2 deconvolution algorithm. Beside the convective ridge, they identified a local maxima in the ellipse representing the acoustic domain. The origin of the acoustic peaks in both experiments is still a subject of controversy. For example, the proximity of the trailing egde of the flat plate in the experiment of Ehrenfried & Koop (2008) can generate a scattered acoustic field, which is much more efficient than the direct boundary layer noise, and the confined character in the experiment of Arguillat *et al.* (2010) can induce resonance modes.

5.1. *Method for computing the spectra and resolution characteristics*

When the wall is plane and the boundary layer is growing slowly, the pressure fluctuations can be considered statistically stationary in time and homogeneous in x_1- and

x_3-directions. The space-time correlation function defined as:

$$R_{pp} = \langle p(\mathbf{x}, t) p(\mathbf{x} + \boldsymbol{\xi}, t + \tau) \rangle$$

where $\langle\ \rangle$ indicates an ensemble average, depends only on the spatial separations $\boldsymbol{\xi} = (\xi_1, 0, \xi_3)$ and on the time delay τ, and is therefore denoted $R_{pp}(\xi_1, \xi_3, \tau)$. In experiments, the frequency spectra are generally obtained directly by Fourier transform of the signal at one point, but the wavenumber-frequency spectra are deduced from multipoint space-time correlations, by using microphone arrays as in Panton & Robert (1994), Arguillat *et al.* (2010), or Ehrenfried & Koop (2008) for instance. When a numerical database is used, as in Kim (1989), Choi & Moin (1990), Chang *et al.* (1999), Viazzo *et al.* (2001), or Hu *et al.* (2006*b*), the wavenumber-frequency spectra are rather preferentially calculated by a three-dimensional Fourier transform $\hat{p}$:

$$\hat{p}(k_{1_m}, k_{3_q}, f_s) = \frac{1}{N_t} \sum_{r=0}^{N_t-1} \left\{ \frac{1}{N_{x_3}} \sum_{p=0}^{N_{x_3}-1} \left[\frac{1}{N_{x_1}} \sum_{l=0}^{N_{x_1}-1} p(x_{1_l}, x_{3_p}, t_r) \mathrm{e}^{-ik_{1_m} x_{1_l}} \right] \mathrm{e}^{-ik_{3_q} x_{3_p}} \right\} \mathrm{e}^{i2\pi \frac{rs}{N_t}} \quad (5.1)$$

with $k_{1_m} = m\Delta k_1$, $k_{3_q} = q\Delta k_3$ for the point corresponding to the three integers (m, q, s). The wavenumber-frequency spectrum is then defined by:

$$\Phi_{pp}(k_{1_m}, k_{3_q}, f_s) = \mathcal{E} \left\{ \lim_{L_{x_1}, L_{x_3}, L_t \to \infty} \frac{1}{L_{x_1} L_{x_3} L_t} \frac{\hat{p}\, \hat{p}^*}{2\pi \Delta k_1 \Delta k_3 \Delta f} \right\} \quad (5.2)$$

with $L_{x_1} = N_{x_1}\Delta x_1$, $L_{x_3} = N_{x_3}\Delta x_3$, $L_t = N_t \Delta t$, $\Delta k_1 = 2\pi/L_{x_1}$, $\Delta k_3 = 2\pi/L_{x_3}$, and $\Delta f = 1/L_t$. The asterisk denotes the complex conjugate. To improve the statistical properties of the expectation operator $\mathcal{E}$, the spectrum is obtained by the average over N_{seg} time segments with 50% overlap. Before a Fourier transform is taken of each segment, the mean value is subtracted and a Hann window is applied; therefore a factor of 8/3 has to be applied to compensate for the Hann window. The same windowing is applied in the streamwise direction which is not homogeneous. The one-dimensional spectra are

obtained by integrating the 3-D spectrum. For instance, the one-sided ($\omega > 0$) point spectrum is:

$$\phi(\omega) = \frac{1}{\pi} \int_{-\infty}^{\infty} \int_{-\infty}^{\infty} \Phi_{pp}(k_1, k_3, f)\, dk_1 dk_3 \tag{5.3}$$

Note that the $1/2\pi$ factor in (5.3) results from the use of the frequency f rather than the angular frequency $\omega = 2\pi f$ in the expression (5.2) of the 3-D spectrum. Moreover, a subsequent factor 2, is used for the single-point spectrum for comparison with the one-sided version generally used in experiments. The mean square of the pressure fluctuations is then calculated by:

$$\overline{p^2} = \int_0^{\infty} \phi(\omega)\, d\omega \tag{5.4}$$

Once the statistical steady state is reached, the wall pressure is stored during 585 000 iterations every 30 time steps of the Navier-Stokes solver ($\Delta t u_\tau/\delta_{\text{ref}} \simeq 1.1 \times 10^{-3}$). The total time of storage corresponds to $L_t u_\tau/\delta_{\text{ref}} = 22.08$, or $L_t U_\infty/\delta^*_{\text{ref}} = 2968$. The 19 500 samples are divided in N_{seg}=11 overlapping segments, each containing 3250 samples. The frequency resolution is $\Delta\omega = 1.71 u_\tau/\delta_{\text{ref}} = 0.013 U_\infty/\delta^*_{\text{ref}}$, and the maximum frequency is $\omega_{\max} = 5549 u_\tau/\delta_{\text{ref}} = 41 U_\infty/\delta^*_{\text{ref}}$. The frequency cut-off due to the spatial resolution is however far lower. By estimating roughly that the spatial scheme is able to resolve spatial structures discretised by four points (Bogey & Bailly (2004)), the wavenumber cut-off is $k_{\text{cut-off}} = 2\pi/4\Delta x = 23.6/\delta_{\text{ref}} = 4.1/\delta^*_{\text{ref}}$. Using the Taylor hypothesis with U_c=0.6, we estimate a cut-off frequency $\omega_{\text{cut-off}} = 335 u_\tau/\delta_{\text{ref}} = 2.5 U_\infty/\delta^*_{\text{ref}}$. The wavenumber resolution is $\Delta k_1 = 2\pi/L_{x_1} = 0.085/\delta_{\text{ref}} = 0.015/\delta^*_{\text{ref}}$ in the streamwise direction and covers a range $0 \leqslant k_1\delta_{\text{ref}} \leqslant 94.6$ ($0 \leqslant k_1\delta^*_{\text{ref}} \leqslant 16.5$). In the spanwise direction, $\Delta k_3 = 2\pi/L_{x_3} = 1.82/\delta_{\text{ref}} = 0.32/\delta^*_{\text{ref}}$, and $0 \leqslant k_3\delta_{\text{ref}} \leqslant 236.6$ ($0 \leqslant k_3\delta^*_{\text{ref}} \leqslant 41.4$).

5.2. *Frequency power spectrum and mean square pressure*

The single-point spectra for successive longitudinal locations are depicted in figure 13 with different scalings. Numerous authors (Blake (1986*a*); Farabee & Casarella (1991); Goody (2004); Hu *et al.* (2006*b*)) have attempted to find an universal scaling for wall pressure frequency spectra, but the choice is not unique. When the inner variables are used, as in figure 13(a), the high-frequency part of the spectra are seen to collapse to some degree. The different spectra superimpose well with experiments in the intermediate range $0.1 \leqslant \omega\nu/u_\tau^2 \leqslant 0.6$. For very high frequencies a decay law with ω^{-5} is expected. This law is satisfied by the model of Goody (2004) which has been plotted with the black dashed line. The semi-empirical model of Goody (2004) is an extension of the Chase-Howe model (Chase (1987); Howe (1998)). To take account of the Reynolds number dependence, Goody proposed the following semi-empirical formula :

$$\frac{\phi(\omega)U_\infty}{\tau_w^2\delta} = \frac{C_2(\omega\delta/U_\infty)^2}{\left[(\omega\delta/U_\infty)^{0.75}+C_1\right]^{3.7}+\left[C_3R_T^{-0.57}(\omega\delta/U_\infty)\right]^7}$$

where $C_1 = 0.5$, $C_2 = 3$ and $C_3 = 1.1$ are empirical constants, $R_T = (\delta/U_\infty/(\nu/u_\tau^2))$ is the ratio of the outer to inner boundary layer time scale, which represents the effect of the Reynolds number, since $R_T \propto u_\tau\delta/\nu$. The model has been plotted for $R_T = 20$, which would correspond to Re_θ=1500. The experimental spectra from the works of Gravante *et al.* (1998), Schewe (1983), and Farabee & Casarella (1991) are in fair agreement with the model of Goody for $\omega\nu/u_\tau^2 \geqslant 0.01$. For very high frequencies, the spectra from the LES fall off too fast, and do not follow the ω^{-5} decay law. In fact, the vertical thick dashed line indicates the frequency cut-off of the simulation as defined in the previous section, and thus explain the discrepancies for $\omega\nu/u_\tau^2 \geqslant 0.67$. The good collapse of the different spectra in the high-frequency range with inner scaling is directly related to the fact that the smaller scales develop near the wall. The use of outer variables in the other

figures allows a good collapse at middle frequencies. No significant difference is noted between figure 13(b) and (c), where δ or δ^* are used as length scales, and U_∞ or u_τ as velocity scales, suggesting that the good collapse in the intermediate range is rather linked to the length scale, which characterizes the size of the turbulent structures associated with those frequencies. The ω^{-1} law followed by a $\omega^{-7/3}$ law invoked by some authors are hardly distinguishable in the present case since the Reynolds number is low, which is also the case in all the numerical databases analysed by Kim (1989), Choi & Moin (1990), Chang *et al.* (1999), Viazzo *et al.* (2001), or Hu *et al.* (2006*b*). The trends of the spectra with increasing Reynolds numbers are indicated by an arrow in figure 13(b)(c)(d), and conform with the observations of Gravante *et al.* (1998) or the model ofGoody (2004). It is also noted that the levels and the maximum of the spectra are in fair agreement with the model and other published measurements. The theoretical ω^2 law at very low frequencies, only verified in the experiments of Farabee & Casarella (1991) (figure 13(c)), is not visible in the present spectra. Recent experiments by Beresh *et al.* (2011) also do not support the ω^2 dependence. We may not explore a sufficiently low frequency range. The use of the dynamic pressure $Q_\infty = \frac{1}{2}\rho_\infty U_\infty^2$ rather than the wall shear stress τ_w as a pressure scale in the last plot of figure 13(d) has been suggested by Farabee & Casarella (1991) to collapse the spectra at the very low frequencies. A rather good superposition is observed, with the exception of the spectra at the lowest Reynolds number Re_θ=848. We can argue that this corresponds to a location where the flow is still transitional just after the small step used to ignite the turbulent motions.

The mean square pressure is evaluated by using (5.4). We find $p_{\mathrm{rms}}/\tau_w \simeq 2.4$ by using a median value for the wall shear stress. This result is in fair agreement with the value of 2.35 reported in the DNS of Spalart (1988), or 2.5 in the experiments of Schewe (1983) for similar Reynods number ($\mathrm{Re}_\theta \simeq 1400$, $\mathrm{Re}_\tau \simeq 500$). The model proposed by Viazzo

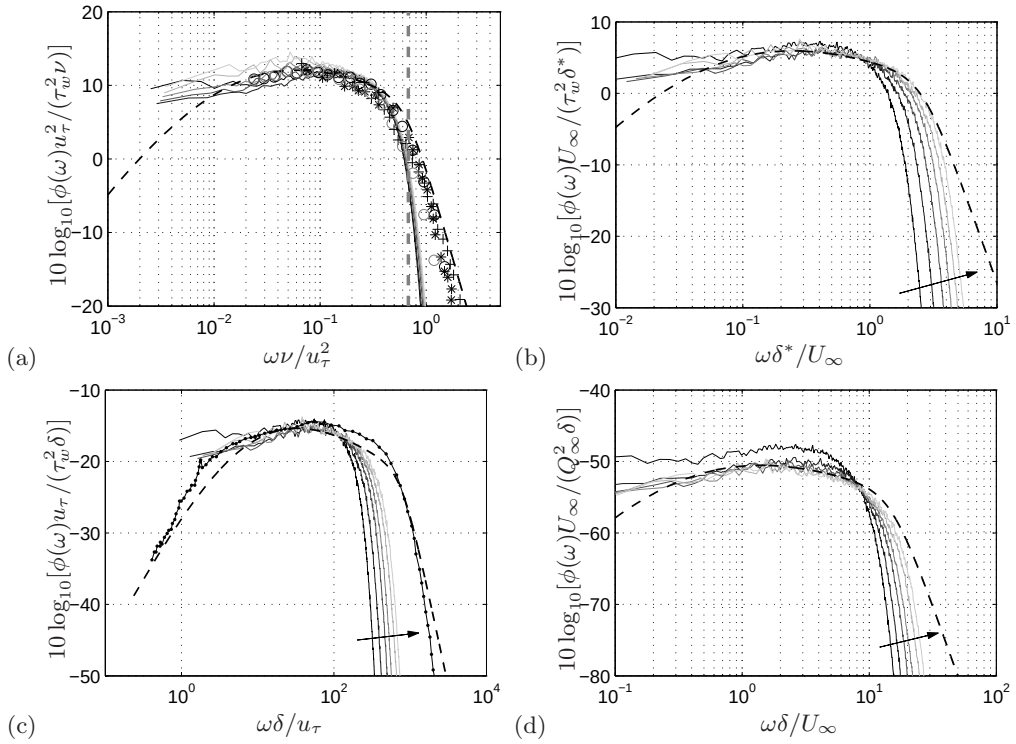

FIGURE 13. Frequency power spectra of wall pressure for successive streamwise absissae: —— $x_1/\delta^*_{\rm ref}$=75.9 (Re$_\theta$=848); —— $x_1/\delta^*_{\rm ref}$=151.8 (Re$_\theta$=1180); —— $x_1/\delta^*_{\rm ref}$=227.8 (Re$_\theta$=1491); —— $x_1/\delta^*_{\rm ref}$=303.7 (Re$_\theta$=1781); —— $x_1/\delta^*_{\rm ref}$=379.6 (Re$_\theta$=2058); —— $x_1/\delta^*_{\rm ref}$=455.6 (Re$_\theta$=2328). (a) Scaling by inner variables: τ_w as pressure scale and ν/u_τ^2 as timescale. Experimental spectra are superimposed: ++ Gravante *et al.* (1998) (Re$_\theta$=2953); ** Farabee & Casarella (1991) (Re$_\theta$=2945); oo Schewe (1983) (d=2 mm, Re$_\theta$=1400); ooSchewe (1983) (d=4 mm, Re$_\theta$=1400). The semi-empirical model of Goody (2004) for R_T=20 is plotted with a black dashed line, and the vertical dashed line indicates the frequency cut-off of the LES. (b) Scaling by outer variables: τ_w as pressure scale and $\delta^*_{\rm ref}/U_\infty$ as timescale. The arrow show the increasing longitudinal locations. – – –: Goody's model (R_T=20). (c) Scaling by outer variables: τ_w as pressure scale and $\delta_{\rm ref}/u_\tau$ as timescale. The measurements of Farabee & Casarella (1991) for U_∞=15 m/s are superimposed (•••), along with Goody's model for R_T=47.11 (– – –). (d) Scaling by outer variables: the dynamic pressure $Q_\infty = \frac{1}{2}\rho_\infty U_\infty^2$ as pressure scale and $\delta_{\rm ref}/U_\infty$ as timescale. – – –: Goody's model (R_T=20).

et al. (2001), which take into account the theoretical contributions of each frequency ranges (low, medium, high), is also used for comparison:

$$p_{\rm rms}^2/\tau_w^2 = 3 + 2\ln({\rm Re}_\tau/250)$$

where the mean value along the computational domain is used for ${\rm Re}_\tau(\simeq 560)$, which yields 2.15. A still lower value of 1.9 is given in the simulations of incompressible channel flow at ${\rm Re}_\tau \simeq 400$ by Kim (1989) (DNS) and at ${\rm Re}_\tau \simeq 640$ by Viazzo *et al.* (2001) (LES). This decrease of pressure fluctuations seems therefore rather related to the confined geometry than to the grid resolution. It must be noted that the too rapid decay at high frequencies in the present simulation is not penalizing for the subsequent analysis since the good estimation of the mean square pressure indicates that the energetic contribution of the high-frequency region is small. For instance, the mean-square pressure predicted by the Goody model values above the cutt-off frequency represents 6% of $p_{\rm rms}$ over the whole frequency range.

5.3. *Broad-band correlations*

In the present study, the space-time correlation function $R_{pp}(\xi_1, \xi_3, \tau)$ is obtained by an inverse Fourier transform of the wavenumber-frequency spectral densities (Wiener-Khintchine theorem). This is an efficient way to compute the correlation from the Fourier transforms of the different signals when a large number of points is involved, by taking advantage of the FFT algorithm. The current grid at the wall is indeed $n_1 = 1120 \times n_3 = 131$ points. The first 100 points in the vicinity of the small step at the upstream end, and 150 points at the downstream end, where grid stretching is used, have been discarded. The reduced grid (x_1, x_3) is thus regular.

Figure 14(a) shows a map of the spatial correlation $R_{pp}(\xi_1, \xi_3, 0)$ at zero time delay. The resulting pattern indicates that at small spacings the wall pressure field appears

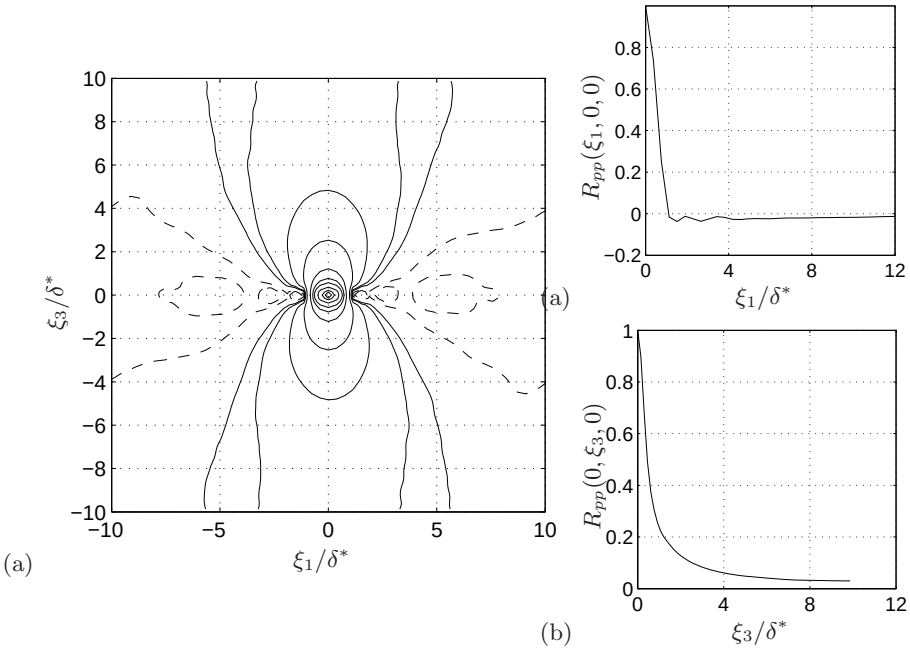

FIGURE 14. Contours of constant space correlation, $R_{pp}(\xi_1, \xi_3, 0)$ of the wall pressure field (a). 10 positive isocontours (solid lines): 0.01, 0.02, 0.05, and 0.1 to 0.9 every 0.1; and 3 negative isocontours (dashed lines): -0.01, -0.02, -0.05. Space correlations of the wall pressure $R_{pp}(\xi_1, 0, 0)$ along the streamwise direction (b), and $R_{pp}(0, \xi_3, 0)$ along the spanwise direction (c).

nearly isotropic. The isocorrelation curves are elongated in the spanwise direction, in good agreement with similar maps provided by Bull (1967). Spatial correlations in the lateral and longitudinal directions are depicted in figure 14. The rapid coherence loss in the longitudinal direction is clearly visible in figure 14(b). The curve becomes and remains negative for spatial separation slightly greater than $\xi_1/\delta^*_{\text{ref}}$=1. The same behavior was observed by Bull (1967) but the negative part began at $\xi_1/\delta^*_{\text{ref}}$=3.9. The scale in the transverse direction indicated by figure 14(c) exceeds that in the streamwise direction, and is in fairly good agreement with the measurements of Willmarth & Woolridge (1962) and Bull (1967). The lateral correlation remains positive.

A way to evaluate the convection speed is to follow the maxima of the longitudinal space-time correlation for different fixed space increments ξ_1 as a function of the time

delay, as illustrated in figure 15. An envelop curve is drawn tangent to the peaks of R_{pp}, defining a function $\xi_1 = f(\tau)$. The average broadband convection velocity is then defined as:

$$\bar{U}_c(\xi_1) = \frac{\xi_1}{\tau}$$

and is plotted with the circles in figure 16(a). The average velocity varies from $0.6U_\infty$ for zero separation to $0.84U_\infty$ for large separations. Willmarth & Woolridge (1962) indicate values of 0.53 at small ξ_1 and 0.83 at large ξ_1, and Bull (1967) reported values of 0.53 and 0.825 respectively. An instantaneous broadband convection velocity may be defined as:

$$U_c(\xi_1) = \frac{d\xi_1}{d\tau}$$

The derivative is evaluated by the slope of the curve corresponding to minimum decay rate of the space-time correlation, plotted in figure 16(b). The instantaneous velocity U_c is reported in figure 16(a) (dashed line). The increase with streamwise separation is in excellent agreement with the measurements of Willmarth & Woolridge (1962), Bull (1967), or Blake (1970). The instantaneous convection velocity approaches $0.85U_\infty$. This reflects the decay of slower small-scale pressure sources, and the gradual predominance of higher-speed sources for large distances.

5.4. *Wall pressure coherence*

The coherence is evaluated for our LES database by first evaluating the cross-spectra by a two-dimensional spatial inverse transform of the wavenumber-frequency spectra. A cross-spectrum is obtained for each frequency, and is a complex function composed of a co-spectrum and a quad-spectrum:

$$S_{pp}(\xi_1, \xi_3, \omega) = C(\xi_1, \xi_3, \omega) - iQ(\xi_1, \xi_3, \omega)$$

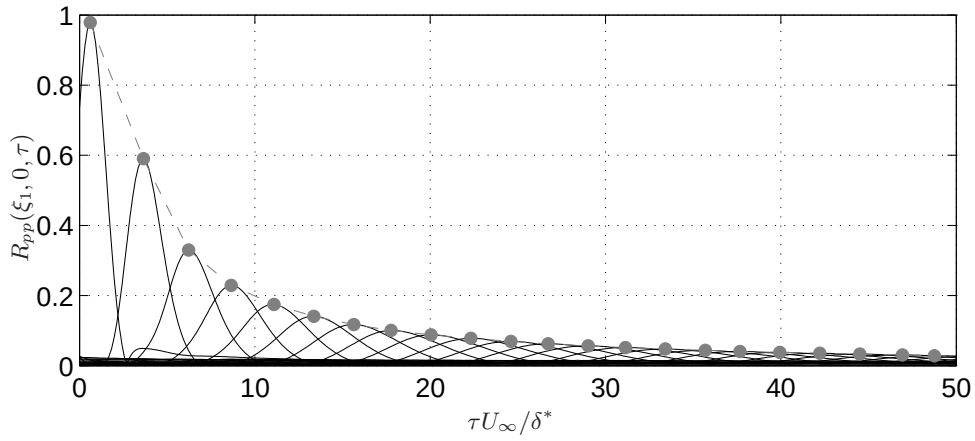

FIGURE 15. Peaks of the longitudinal space-time correlation for increasing space increments ξ_1/des=1.9 as a function of the nondimensionalised time increment $\tau U_\infty/\delta^*$. The grey bullets show the maximum location.

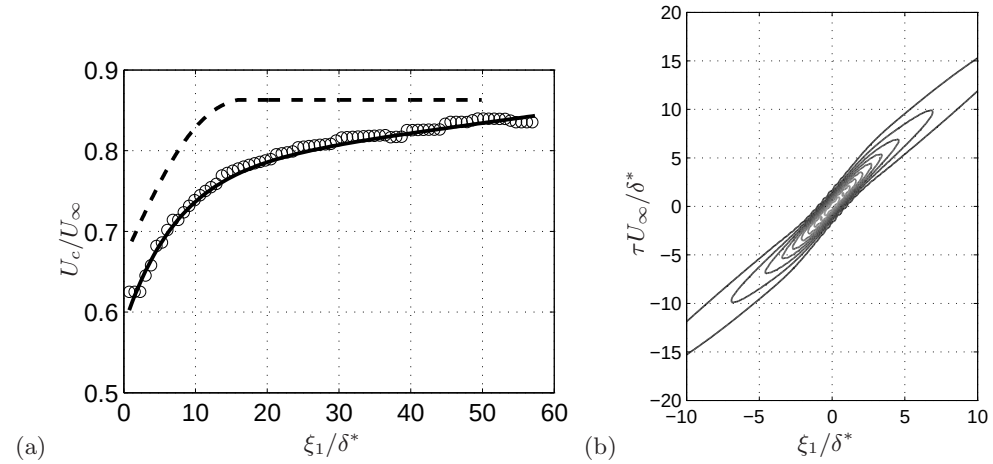

FIGURE 16. Broad-band convection velocities. (a) Average $\bar{U}_c$ (ooo) and instantaneous U_c (- - -) convection velocities as a function the longitudinal separaction distance. The solid line is a curve fitting of the average velocity. (b) Contour map of the longitudinal space-time correlation of the wall pressure $R_{pp}(\xi_1, 0, \tau)$. Contour levels are -0.01, -0.1 to 0.9 with intervals 0.1.

A phase angle can be introduced as $\alpha(\xi_1, \xi_3, \omega) = \tan^{-1}(Q(\xi_1, \xi_3, \omega)/C(\xi_1, \xi_3, \omega))$, and is plotted in figure 17(a). The broadband analysis of the previous section has provided a mean value of the convection properties across the entire boundary layer. Since the

convection velocity will depend on the size of the turbulent structures and on their vertical position inside the boundary layer, it is expected bo be frequency-dependent. Bull (1967) and Blake (1970) suggest to use narrow-band correlations, that is by performing the analysis for a given narrow frequency band. This allows to estimate an effective velocity for eddies of various scales, and thus to estimate their average life-times. In the same way, cross-spectra yield a phase speed $U_{cp} = \omega\xi_1/\alpha$, depending on the frequency. It is depicted in figure 17(b) and 18(a), and can be compared to the narrow-band correlations measured by Blake (1970). A comparison with the experiments of Farabee & Casarella (1991), and Leclercq & Bohineust (2002) is proposed in figure 18(a). The phase velocities are seen to increase rapidly from zero as the frequency is increased and then reach a plateau. For large separations, the increase is abrupt and an asymptote around $0.75U_\infty$ is reached. The value of this limit is also in fair agreement with the measurements of Bull (1967) and Blake (1970). For the smallest separation plotted, a phase velocities of 0.55 is noted indicating that the less correlated structures, probably small scales, are convected more slowly. This is coherent with the picture of smaller scales closer to the wall. Similar results are also reported in the analysis of the LES of incompressible channel flow by Viazzo *et al.* (2001). These authors reported a peak value around $\omega\delta^*/U_\infty \approx 0.3$, which is also detectable in the present study, and is also in qualitative agreement with the experiments of Blake (1970).

The coherence Γ is defined as $|S_{pp}(\xi_1, \xi_3, \omega)|/|S_{pp}(0, 0, \omega)|$. The longitudinal and transverse coherences are represented in figure 19 versus the phase angle. A good collapse is observed at high frequencies for the different separations ξ_i. Since the work of Corcos (1963), the coherence has frequently been assumed to be a decreasing function of a Strouhal number, based on the separation ξ_i, the pulsation ω, and a characteristic velocity. Corcos has taken exponentials in the x_1- and x_3-directions, and modeled the loss of

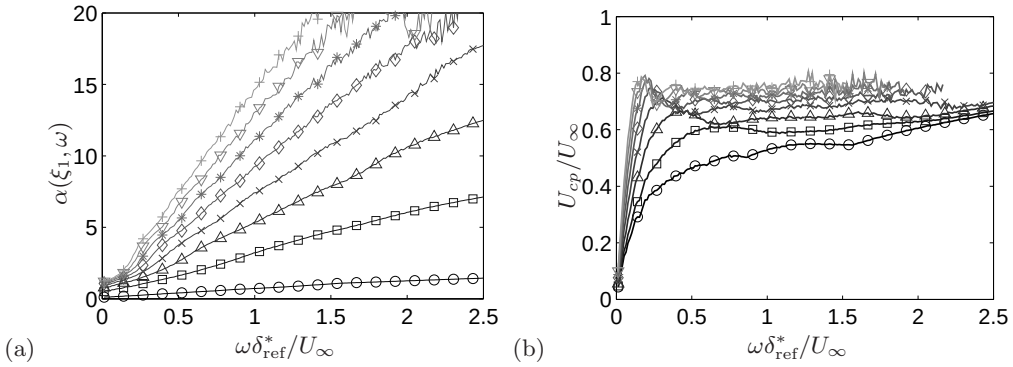

FIGURE 17. (a) Phase angle $\alpha(\xi_1, 0, \omega)$ as a function of the nondimensional frequency for successive streamwise separations $\xi_1/\delta^*_{\rm ref}$=0.38 (o), 1.14 (□), 1.90 (△), 2.66 (×), 3.42 (⋄), 4.18 (*), 4.93 (▽), 5.69 (+), 6.45 (o). (b) Phase velocities U_{cp} versus frequency for the same streamwise separations.

coherence by the product:

$$S_{pp}(\boldsymbol{\xi},\omega) = \phi(\omega)\, \mathrm{e}^{-\frac{\omega|\xi_1|}{\alpha_1 U_c}}\, \mathrm{e}^{-\frac{\omega|\xi_3|}{\alpha_3 U_c}}\, \mathrm{e}^{i\omega\xi_1/U_c} \tag{5.5}$$

Exponential curves $\exp(-\omega|\xi_i|/(\alpha_i U_{cp}))$ fit well the high-frequency coherence loss. The small scales responsible for the high-frequency content are indeed rapidly destroyed as they are convected. The values $1/\alpha_1$=0.12 and $1/\alpha_3$=0.72 deduced from figure 19 are in very good agreement with the values 0.11 and 0.714 obtained by Corcos (1963) from miscellaneous experimental databases, or 0.116 and 0.7 reported by Blake (1970). However, as noted by several authors, such as Bull (1967), Farabee & Casarella (1991), or Leclercq & Bohineust (2002), the coherence does not tend to unity as the frequency tends to zero as observed in figure 18(b), where the data of Leclercq & Bohineust (2002) have been added. This behavior is related to the limitation in eddy size imposed by the boundary layer thickness, and the alteration of large strutures by the TBL shear.

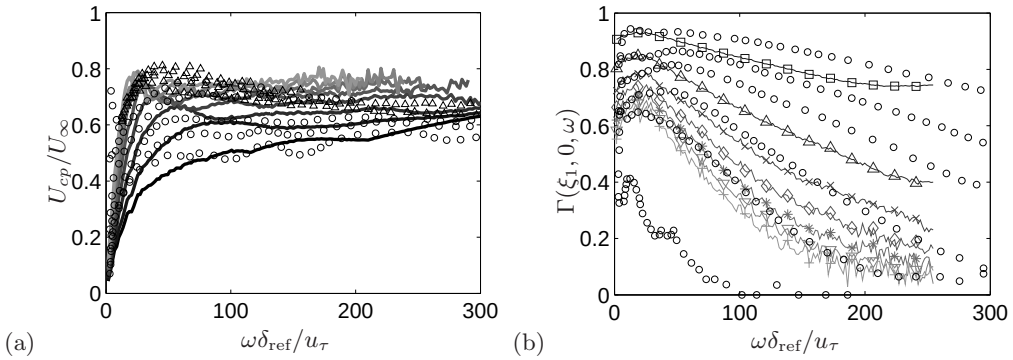

FIGURE 18. (a) Phase velocities versus frequency compared to the experimental results of Farabee & Casarella (1991) at Re_θ=2945 ($\triangle$), and Leclercq & Bohineust (2002) at Re_θ=7467 (o). (b) Coherence versus nondimensional frequency for successive streamwise separations compared to measurements by Leclercq & Bohineust (2002) (o). The successive streamwise separations are given in figure 19 for the LES simulation. They are ξ_1/δ=0.10, 0.24, 0.42, 0.9, and 1.63 in Leclercq and Bohineust's experiment, and $0.21 \leqslant \xi_1/\delta \leqslant 5$ in Farabee and Casarella's experiment.

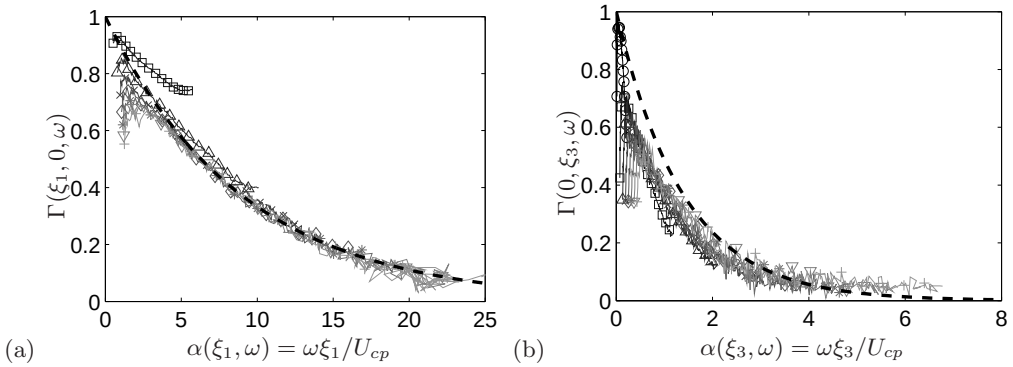

FIGURE 19. Coherence Γ as a function of the phase angle: (a) for successive streamwise separations $\xi_1/\delta^*_{\rm ref}$=1.90 ($\square$), 3.42 ($\triangle$), 4.94 ($\times$), 6.45 ($\diamond$), 7.97 (*), 9.49 ($\triangledown$), 11.01 (+); (b) for successive spanwise separations $\xi_3/\delta^*_{\rm ref}$=0.15 (o), 0.76 ($\square$), 1.37 ($\triangle$), 1.97 ($\times$), 2.58 ($\diamond$), 3.19 (*), 3.80 ($\triangledown$), 4.40 (+). An exponential fit $\exp(-\omega|\xi_i|/(\alpha_i U_{cp}))$ (- - -) is superimposed in the ξ_1-($\alpha_1 = 1/0.12$) or ξ_3-direction ($\alpha_3 = 1/0.72$).

5.5. *Wavenumber-frequency spectra*

The wavenumber-frequency spectrum is obtained by three-dimensional fast Fourier transform as explained in §5.1. The map of a slice of the three-dimensional spectrum for $k_3 = 0$

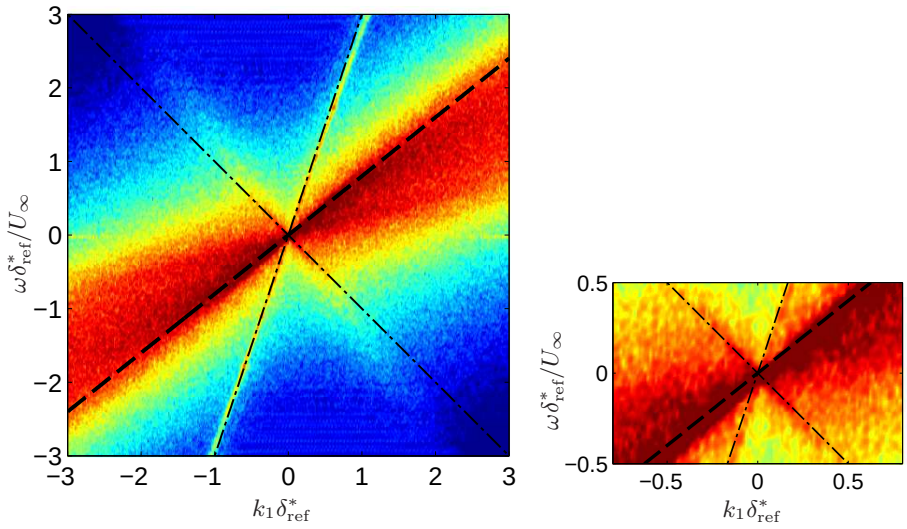

FIGURE 20. Map of the frequency wavenumber spectrum $\Phi_{pp}(k_1, 0, f)$ of the wall pressure fluctuations in dB (ref 1 Pa^2 m/Hz) with levels between -16 and -6 dB. The thick dashed line represents the relation $k_c = \omega/U_c$ with $U_c = 0.6U_\infty$. The dash-dotted lines denotes the convected acoustic wavenumber $\kappa_0 = \omega/(U_\infty \pm c_\infty)$. Closeview on the right; the dashed line now represents the relation $k_c = \omega/U_c$ with $U_c = 0.8U_\infty$.

in figure 20 presents a principal peak that characterizes the convected nature of the wall-pressure field. The mean convection velocity is retrieved (black dashed line in figure 20). As already observed by Wills (1970), Panton & Robert (1994), or Hu *et al.* (2002), the convection ridge is asymmetric, with a tendency to broaden at higher frequencies. This broadening for increasing streamwise wavenumbers after the location of the convective peak is clearly noted in the individual spectra of figure 21, and is induced by the reduction of the correlation lengths at high frequencies. The asymmetry also indicates more energy in the forward moving waves. An acoustic activity can be noted near the location of the acoustic wavenumbers $\kappa_0 = \omega/(U_\infty + c_\infty)$. The fine peak is more intense at high frequencies $\omega\delta^*/U_\infty > 1$. A more smeared peak for negative streamwise wavenumbers $\kappa_0 = \omega/(c_\infty - U_\infty)$ is detectable, and corresponds to waves propagating towards the upstream direction. The closeview in the right of figure 20 shows that the acoustic

waves in the direction opposite to the flow have a greater level at low frequenices, so they correspond to the main noise radiation identified by direct inspection. The acoustic peaks are clearly seen in the cuts at fixed frequencies in figure 21. A broadband hump is apparent for negative streamwise wavenumbers, which is more sharp at the low frequencies of interest, *e.g.* $\omega\delta^*_{\rm ref}/U_\infty$=0.25. The wavenumber-frequency spectrum in the k_1-k_3 plane is represented in figure 22(a) for $\omega\delta^*/U_\infty$=0.32, and clearly shows the convective ridge. Some noise is visible on the contours because of the reduced spanwise extent in the simulation and the limited time duration but its shape is satisfactory and exhibits the well-known convective crest. In this representation, the range of supersonic wavenumber $k=\sqrt{k_1^2+k_3^2}<\omega/c_\infty$ defines the acoustic domain, bounded by the circle $k=\kappa_0$. When a mean flow, defined by a Mach number M, is present, the supersonic wavenumbers correspond to $(\kappa_0-k_1{\rm M})^2-(k_1^2+k_3^2)>0$. Noting $\beta=\sqrt{1-M^2}$ the Prandtl-Glauert parameter, the acoustic domain is represented in the wavenumber space by the interior of the ellipse:

$$\frac{\left(k_1+\kappa_0{\rm M}/\beta^2\right)^2}{\left(\kappa_0/\beta^2\right)^2}+\frac{k_3^2}{\left(\kappa_0/\beta\right)^2}=1 \tag{5.6}$$

with center at $(-\kappa_0{\rm M}/\beta^2,0)$, major radius κ_0/β^2, and minor radius κ_0/β. As seen in figure 22(a), this ellipse is already merged with the convective crest at $\omega\delta^*_{\rm ref}/U_\infty$=0.32 (slightly greater than the end of the low-frequency bump, $\omega\delta^*_{\rm ref}/U_\infty$=0.2). The map in figure 22(b) at $\omega\delta^*_{\rm ref}/U_\infty$=1.69 is representative of the high-frequency acoustic activity noted in figure 20. Small peaks are visible near the upper limit of the acoustic domain in figure 21 for $\omega\delta^*_{\rm ref}/U_\infty$=1.69 and 2.54. Since the ellipse bounding the acoustic domain is now almost separated from the convective ridge, it is possible to discern the peaks in the acoustic domain in figure 22(b). This frequency is however well above the range of interest, and pertains to the low-level high-frequency emissions. Due to the relatively high speed of the flow, and the large-wavelength acoustic waves, figure 22(a) is more

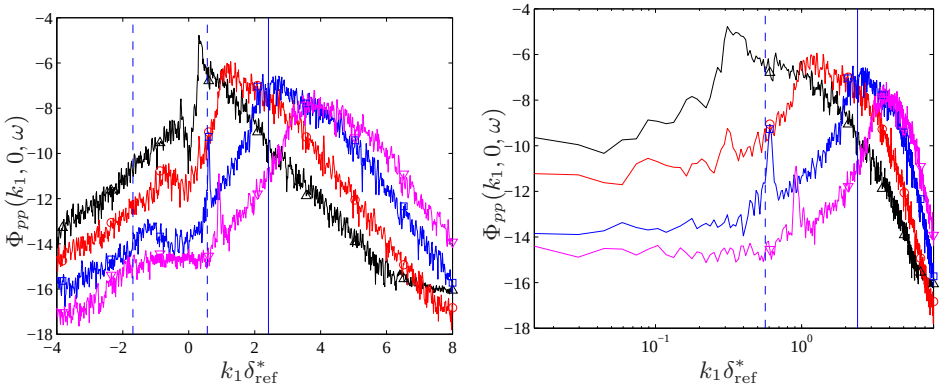

FIGURE 21. Wavenumber frequency spectra in dB (ref 1 Pa^2 m/Hz) for different fixed nondimensional frequency $\omega\delta^*/U_\infty$: 0.25 (—— △), 0.85 (—— o), 1.69 (—— □), 2.54 (—— ▽). At the frequency $\omega\delta^*/U_\infty$=0.85, the solid vertical line indicates the convective wavenumber $k_c = \omega/U_c$, and the dashed vertical line indicates the convected acoustic wavenumber.

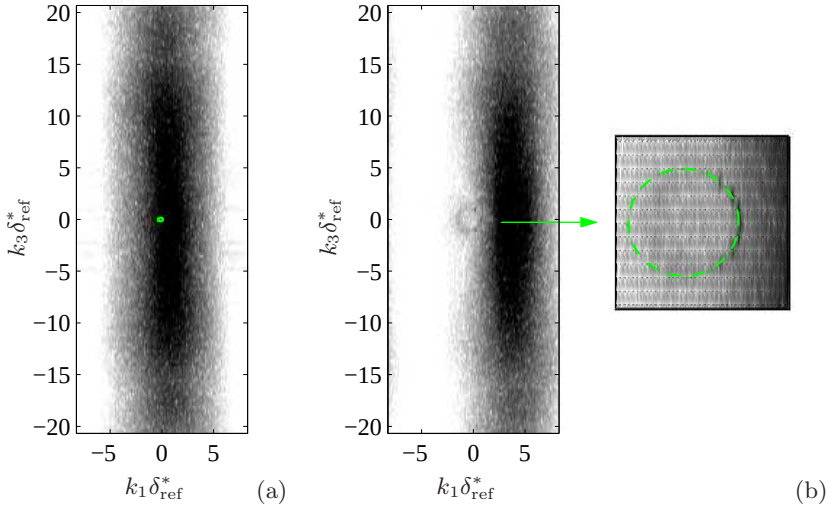

FIGURE 22. Contour plots of the frequency wavenumber spectrum $\Phi_{pp}(k_1, k_3, \omega)$ of the wall pressure fluctuations with a logarithmic colorscale: (a) $\omega\delta^*/U_\infty$=0.32; (b) $\omega\delta^*/U_\infty$=1.69. The ellipse indicates the boundary of the acoustic domain defined by (5.6).

representative, and indicates that the acoustic domain is merged within the aerodynamic peak in this representation. The acoustic contribution is nonetheless identifiable in k_1-ω slices.

6. Conclusions

We have computed directly the noise radiated from a turbulent boundary layer, by performing a compressible large eddy simulation with a very long domain in the streamwise direction and non reflecting boundary conditions. A small step is used to reach a turbulent state, and is seen to generate spurious high-frequency diffracted waves. The direct computation however provides a picture of the acoustic wavefronts radiated outside the boundary layer. The main finding is that the wavelengths are large, so that the classical assumption that the acoustic waves are related to the most important dynamical structures, such as the hairpin-like vortices, does not hold. in the direction opposite to the flow, due to the important Doppler effect at M=0.5, which is still reinforced for horizontal longitudinal quadrupolar sources. The significant increase of emissions in the upstream direction is also an indication that the sources are compact, and thus correspond to localized vortical events. Large-scale organisations in a turbulent boundary layer is an active field of research, such as packets of hairpin (Adrian *et al.* (2000)), fusion of packets in the spanwise direction (Tomkins & Adrian (2003)), or long meandering structures (Hutchins *et al.* (2011)). The characterisation of vortical events such as the breakdown of these large-scale structures deserves a further study.

The wall pressure beneath the turbulent boundary layer has been studied since it the basis of the great majority of semi-empirical models, used as input for structural analysis. The main features such as spatio-temporal correlation, point spectra, or coherence are in good agreement with previous experimental or numerical databases. In particular, the frequency-wavenumber representation allow a separation between the non-radiating and the radiating components, having supersonic wavenumber and thus a phase speed greater than the sound speed. Peaks near the location of the slender cone bounding the acoustic domain are detectable. Unfortunately, due to a combination of the low-frequency range of

acoustic emission, and the high speed of the flow, the acoustic domain is hardly separated from the convective ridge for the frequencies of interest. The acoustic efficiency is very low (less that 1% of the aerodynamic pressure in our configuration) explaining that it is rapidly merged in the tail of the aerodynamic crest.

The very low efficiency for a flat plate also explains why few experiments are available, and hardly give an indication on the direct acoustic contribution. Of course, thanks to the present numerical approach, we have only obtained results for one particular configuration, and it would be interesting to apply direct noise computations to investigate the effect of the Mach number or of the Reynolds number on the radiated noise. It can also help to identify the vortical events which are the sources of boundary layer noise.

This work was granted access to the HPC resources of IDRIS and CCRT under the allocation 2009-1736 made by GENCI (Grand Equipement National de Calcul Intensif). The authors would like to thank Professor Jean-Christophe Robinet for providing the local stability code.

Appendix A. Sources under a boundary layer flow

The directivity and sound power radiated by a simple source under a boundary layer have been studied by Suzuki & Lele (2003) or Smith & Morfey (2006). In the same manner, a two-dimensional version of the direct solver, presented in §2, is used to characterise the propagation effects for the frequencies of interest. Case D of Suzuki & Lele (2003) is first reproduced to give confidence into the numerical procedure. A Gaussian monopolar source with an amplitude of 1 Pa is embedded in a laminar boundary layer flow with a freestream Mach number M_∞=0.3. The ratio between the acoustic wavelength and the boundary layer thickness is λ/δ=1/1.66. The vertical source position is 0.016λ, yielding a Reynolds number $Re_\delta = 3710$. A 602×522 Cartesian grid is used with

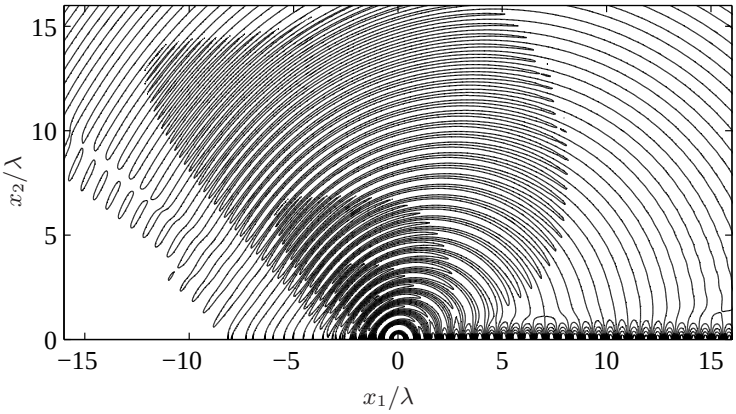

FIGURE 23. Pressure isocontours for case D of Suzuki & Lele (2003) study. The range of contour levels is -0.11 to 0.11 Pa with intervals of 2.75×10^{-2}.

$\Delta x_1 = 3.75 \times 10^{-5}$ m and $\Delta x_{2_{\min}} = 10^{-6}$ m. The mesh is stretched in the vertical direction with a rate of 2.5% for the 130 first grid points and is then regular. Instantaneous pressure isocontours depicted in figure 23 are in good agreement with the results of Suzuki & Lele (2003). In particular, for this relatively high-frequency case, the refracted waves yields a shadow zone upstream of the source, and channeled waves are visible downstream of the source.

Simulations are now conducted by taking exactly the mean flow of the fine-grid LES at M_∞=0.5 with a turbulent mean velocity profile. Two frequencies, already used in the Fourier analysis, namely $\omega\delta^*_{\text{ref}}/U_\infty$=0.033, and 0.20, are tested. The corresponding ratios $\lambda/\delta_{\text{ref}}$ are 66.3 and 10.8 respectively. The 201×201 Cartesian meshgrid has the same mesh sizes as those of the LES study, *i.e.* $\Delta x_1 = 3.75 \times 10^{-4}$ m and $\Delta x_{2_{\min}} = 10^{-5}$ m. The simulations are stopped before the development of flow instabilities. Fluctuating pressure contours for the two frequencies representative of the direct noise generated by a TBL are plotted in figure 24. No channeled waves are present, and the refraction effect, totally negligible at the lowest frequency, remains weak for the highest tested frequency. The influence of the mean flow profile and of the source height on the refraction effect

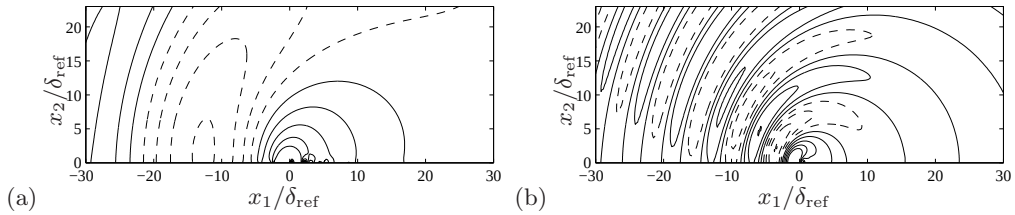

FIGURE 24. Monopolar sources in a turbulent boundary layer flow. The source frequencies are $\omega\delta^*_{\rm ref}/U_\infty$=0.033 (a), and 0.20 (b). The height of the source is set at $0.09\delta_{\rm ref}$. Pressure contour levels are between -0.005 and 0.005 with intervals 0.00125 (a), and between -0.11 and 0.11 with intervals 0.0275 (b).

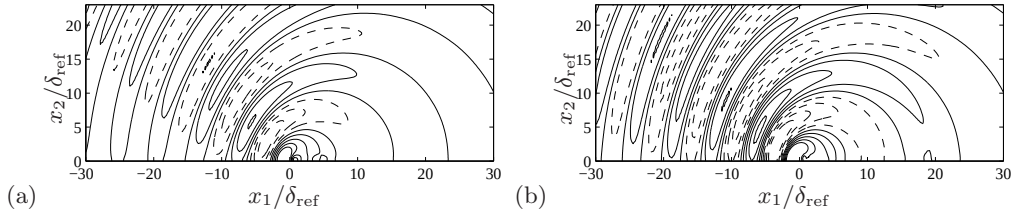

FIGURE 25. Monopolar sources at $\omega\delta^*_{\rm ref}/U_\infty$=0.20: (a) the mean velocity profile corresponds to a laminar flow and the height is $0.09\delta_{\rm ref}$ as in figure 24(c); (b) the mean profile is turbulent as in figure 24(c) and the source is moved away from the wall at $0.37\delta_{\rm ref}$. Contour levels are the same as figure 24(c).

are next investigated in figure 25. When the turbulent profile is replaced by a Blasius profile, the shadow zone is more extended (compare figure 24(b) and 25(a)). Figure 25(b) indicates that the refraction is weakened by moving the source away from the wall. It is thus concluded that the refraction and channeling are negligible in the analysis of the sound directivity in the present turbulent flow configuration.

Propagation effects for higher-order sources are then illustrated in figure 26. Dipoles are obtained by taking two identical sources in opposite phase separated by a small distance $\lambda/20$. When the two sources are aligned in the vertical direction in figure 26(a), the resulting pressure wavefronts are less directional. On the contrary, for an horizontal dipole, *i.e.* two opposite sources on an horizontal line, the Doppler effect is strength-

ened, leading to a lobe oriented in the direction opposite to the flow in figure 26(b). Same conclusions arise for a longitudinal quadrupole, *i.e.* two opposite dipoles on a line. The directivity is more omnidirectional in figure 26(d), than in figure 26(e), where the emission in the upstream direction is increased and low power levels are observed in the downstream part. The convection effect are also important for the case of a lateral quadrupole in figure 26(c), but the overall levels are decreased, because of cancellations arising from the wall reflections. In the analogy of Powell (1960), the normal pressure or shear stress dipoles degenerate into quadrupole, thus reducing their efficiency. Similarly, lateral $T_{ij,i\neq j}$ and vertical longitudinal T_{22} quadrupoles degenerate into octopoles. The dominant sources are thus expected to be the tangential shear stress (horizontal dipole, as in figure 26(b)), and horizontal longitudinal quadrupole (as in figure 26(e)), because these sources are doubled by the reflection. This hierarchy is well retrieved when we applied the Powell analogy with the LES data in Gloerfelt (2010).

REFERENCES

Adrian, R.J., Meinhart, C.D. & Tomkins, C.D. 2000 Vortex organization in the outer region of the turbulent boundary layer. *J. Fluid Mech.* **422**, 1–54.

Arguillat, B. 2006 Etude expérimentale et numérique de champs de pression pariétale dans l'espace des nombres d'onde, avec application aux vitrages automobiles. PhD thesis, Ecole Centrale de Lyon, no 2006-14.

Arguillat, B., Ricot, D., Robert, G. & Bailly, C. 2010 Measured wavenumber-frequency spectrum associated with acoustic and aerodynamic wall pressure fluctuations. *J. Acoust. Soc. Am.* **128** (4), 1647–1655.

Barker, S.J. 1973 Radiated noise from turbulent boundary layers in dilute polymer solutions. *Phys. Fluids* **16**, 1387–1394.

Beresh, S.J., Henfling, J.F., Spillers, R.W. & Pruett, B.O.M. 2011 Fluctuating wall

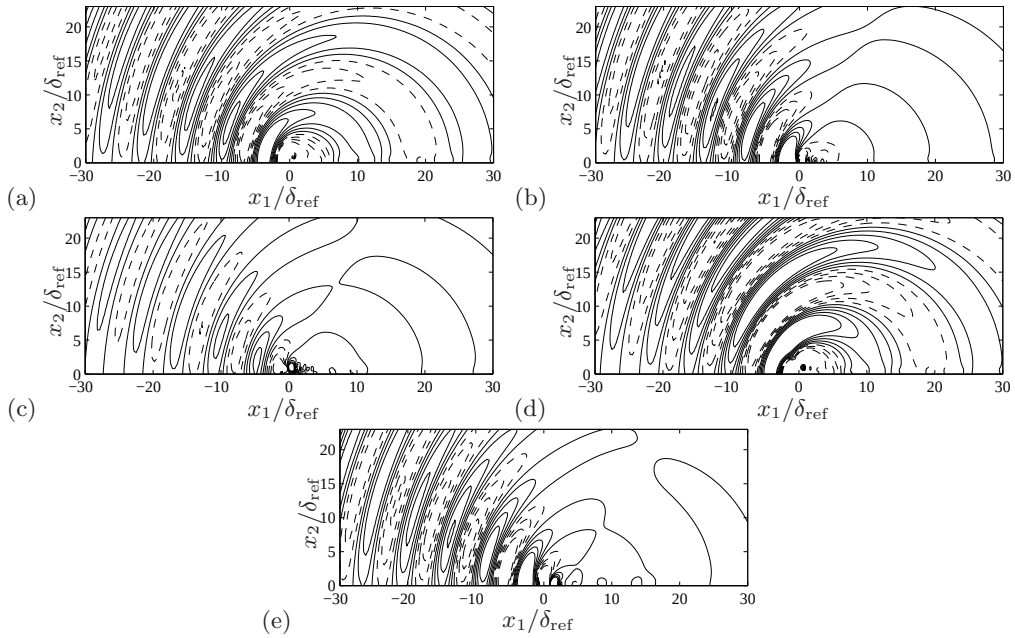

FIGURE 26. Higher-order sources in a turbulent boundary layer flow: (a) vertical dipole; (b) horizontal dipole; (c) lateral quadrupole; (d) vertical longitudinal quadrupole; (e) horizontal longitudinal quadrupole. The source frequency is $\omega\delta^*_{\rm ref}/U_\infty$=0.20, and its height is $0.09\delta_{\rm ref}$. Contour levels are the same as figure 24(c).

pressures measured beneath a supersonic turbulent boundary layer. *Phys. Fluids* **23**, 075110.

BERGERON, R.F. 1974 Acoustic sources in the low Mach number turbulent boundary layer. *J. Acoust. Soc. Am.* **54** (1), 123–133.

BERLAND, J. & GLOERFELT, X. 2008 Investigation of noise radiation from a turbulent boundary layer. *14th AIAA/CEAS AeroAcoustics Conference,* 5-7 May, Vancouver, Canada, AIAA Paper 2008-2802 .

BLAKE, W.K. 1970 Turbulent boundary-layer wall-pressure fluctuations on smooth and rough walls. *J. Fluid Mech.* **44**, 637–660.

BLAKE, W.K. 1986*a* *Mechanics of flow-induced sound and vibration*, , vol. 2: Complex flow-structure interaction, chap. 8, Essentials of turbulent wall-pressure fluctuations, pp. 497–594. Academic Press, Inc.

BLAKE, W.K. 1986*b* *Mechanics of flow-induced sound and vibration*, , vol. 2: Complex flow-

structure interaction, chap. 9, Structural response to turbulent wall flow and random sound, pp. 595–657. Academic Press, Inc.

Bogey, C. & Bailly, C. 2002 Three-dimensional non-reflective boundary conditions for acoustic simulations : far field formulation and validation test cases. *Acta Acustica* **88**, 463–471.

Bogey, C. & Bailly, C. 2004 A family of low dispersive and low dissipative explicit schemes for noise computation. *J. Comput. Phys.* **194**, 194–214.

Bogey, C. & Bailly, C. 2006 Large eddy simulations of round jets using explicit filtering with/without dynamic Smagorinsky model. *International Journal of Heat and Fluid Flow* **27**, 603–610.

Bull, M.K. 1967 Wall-pressure fluctuations associated with subsonic boundary layer flow. *J. Fluid Mech.* **28**, 719–754.

Bull, M.K. 1996 Wall-pressure fluctuations beneath turbulent boundary layers: Some reflections on forty years of research. *J. Sound Vib.* **190** (3), 299–315.

Chang, P., Piomelli, U. & Blake, W. 1999 Relationship between wall pressure and velocity sources. *Phys. Fluids* **11** (11), 3434–3448.

Chase, D.M. 1980 Modeling the wavevector-frequency spectrum of turbulent boundary layer wall pressure. *J. Sound Vib.* **70**, 29–67.

Chase, D.M. 1987 The character of the turbulent wall pressure spectrum at subconvective wavenumbers and a suggested comprehensive model. *J. Sound Vib.* **112** (1), 125–147.

Choi, H. & Moin, P. 1990 On the space-time characteristics fo wall-pressure fluctuations. *Phys. Fluids A* **2** (8), 1450–1460.

Corcos, G.M. 1963 Resolution of pressure in turbulence. *J. Acoust. Soc. Am.* **35**, 192–199.

Curle, N. 1955 The influence of solid boundaries upon aerodynamic sound. *Proc. of the Royal Society of London* **A 231**, 505–514.

Dowling, A.P. 1992 Flow noise on surfaces. In *Modern methods in analytical acoustics: Lectures notes* (ed. D.G. Crighton, A.P. Dowling, J.E. Ffowcs Williams, M. Heckl & F.G. Leppington), pp. 452–509. London: Springer Verlag.

Ehrenfried, K. & Koop, L. 2008 Experimental study of pressure fluctuations beneath a

compressible turbulent boundary layer. *14th AIAA/CEAS AeroAcoustics Conference,* 5-7 May, Vancouver, Canada, AIAA Paper 2008-2800 .

Farabee, T.M. & Casarella, M.J. 1991 Spectral features of wall pressure fluctuations beneath turbulent boundary layers. *Phys. Fluids A* **3** (10), 2410–2420.

Ffowcs Williams, J.E. 1965 Surface-pressure fluctuations induced by boundary-layer flow at finite Mach number. *J. Fluid Mech.* **22**, 507–519.

Ffowcs Williams, J.E. 1982 Boundary-layer pressures and the Corcos model : a development to incorporate low-wavenumber constraints. *J. Fluid Mech.* **125**, 9–25.

Garnier, E., Adams, N. & Sagaut, P. 2009 *Large eddy simulation for compressible flows*. Springer.

Gloerfelt, X. 2010 The link between wall pressure spectra and radiated sound from turbulent boundary layers. *16th AIAA/CEAS AeroAcoustics Conference,* 7-9 June, Stockholm, Sweeden, AIAA Paper 2010-3904 .

Gloerfelt, X. & Berland, J. 2009 Direct computation of turbulent boundary layer noise. *15th AIAA/CEAS AeroAcoustics Conference,* 11-13 May, Miami, Florida, AIAA Paper 2009-3401 .

Gloerfelt, X. & Lafon, P. 2008 Direct computation of the noise induced by a turbulent flow through a diaphragm in a duct at low Mach number. *Computers and Fluids* **37**, 388–401.

Gloerfelt, X. & Le Garrec, T. 2008 Generation of inflow turbulence for aeroacoustic applications. *14th AIAA/CEAS AeroAcoustics Conference,* 5-7 May, Vancouver, Canada, AIAA Paper 2008-2926 .

Goody, M. 2004 Empirical spectral model of surface pressure fluctuations. *AIAA Journal* **42** (9), 1788–1794.

Graham, W.R. 1997 A comparison of models for the wavenumber-frequency spectrum of turbulent boundary layer pressures. *J. Sound Vib.* **206** (4), 541–565.

Gravante, S.P., Naguib, A.M., Wark, C.E. & Nagib, H.M. 1998 Characterization of the pressure fluctuations under a fully developed turbulent boundary layer. *AIAA Journal* **36** (10), 1808–1816.

Greshilov, E.M. & Mironov, M.A. 1983 Experimental evaluation of sound generated by turbulent flow in a hydrodynamic duct. *Sov. Phys. Acoust.* **29**, 275–280.

Gustafsson, F. 1996 Determining the initial states in forward-backward filtering. *IEEE Transactions on Signal Processing* **44** (4), 988–992.

Haddle, G.P. & Skudrzyk, E.J. 1969 The physics of flow noise. *J. Acoust. Soc. Am.* **46** (1), 130–157.

Haj-Hariri, H. & Akylas, T.R. 1985 The wall-shear-stress contribution to boundary-layer noise. *Phys. Fluids* **28** (9), 2727–2729.

Hardin, J.C. 1991 Acoustic sources in the low Mach number turbulent boundary layer. *J. Acoust. Soc. Am.* **90** (2), 1020–1031.

Head, M.R. & Bandyopadhyay, P. 1981 New aspects of turbulent boundary layer structures. *J. Fluid Mech.* **107**, 297–338.

Howe, M.S. 1979*a* The interaction of sound with low Mach number wall turbulence, with application to sound propagation in turbulent pipe flow. *J. Fluid Mech.* **94** (4), 729–744.

Howe, M.S. 1979*b* The rôle of surface shear stress fluctuations in the generation of boundary layer noise. *J. Sound Vib.* **65** (2), 159–164.

Howe, M.S. 1991 Surface pressures and sound produced by turbulent flow over smooth and rough walls. *J. Acoust. Soc. Am.* **90** (2), 1041–1047.

Howe, M.S. 1992 A note on the Kraichnan-Phillips theorem. *J. Fluid Mech.* **234**, 443–448.

Howe, M.S. 1998 *Acoustics of fluid-structures interactions*. Cambridge University Press.

Hu, Z.W., Morfey, C.L. & Sandham, N.D. 2002 Aeroacoustics of wall-bounded turbulent flows. *AIAA Journal* **40**, 465–473.

Hu, Z.W., Morfey, C.L. & Sandham, N.D. 2003 Sound radiation in turbulent channel flows. *J. Fluid Mech.* **475**, 269–302.

Hu, Z.W., Morfey, C.L. & Sandham, N.D. 2006*a* Sound radiation from a turbulent boundary layer. *Phys. Fluids* **18**, 098101.

Hu, Z.W., Morfey, C.L. & Sandham, N.D. 2006*b* Wall pressure and shear stress spectra from direct simulations of channel flow. *AIAA Journal* **44**, 1541–1549.

Hutchins, N., Monty, J.P., Ganapathisubramani, B., Ng, H.C. & Marusic, I. 2011 Three-

dimensional conditional structure of a high-Reynolds-number turbulent boundary layer. *J. Fluid Mech.* **673**, 255–285.

Hwang, Y.F., Bonness, W.K. & Hambric, S.A. 2009 Comparison of semi-empirical models for turbulent boundary layer wall pressure spectra. *J. Sound Vib.* **319** (1-2), 199–217.

Jimenez, J., Hoyas, S., Simens, M.P. & Mizuno, Y. 2010 Turbulent boundary layers and channels at moderate Reynolds numbers. *J. Fluid Mech.* **657**, 335–360.

Kim, J. 1989 On the structure of pressure fluctuations in simulated turbulent channel flow. *J. Fluid Mech.* **205**, 421–451.

Kraichnan, R.H. 1956 Pressure fluctuations in a turbulent flow over a flat plate. *J. Acoust. Soc. Am.* **28** (3), 378–390.

Landahl, M.T. 1975 Wave mechanics of boundary layer turbulence and noise. *J. Acoust. Soc. Am.* **57** (4), 824–831.

Lauchle, G.C. 1980 On the radiated noise due to boundary layer transition. *J. Acoust. Soc. Am.* **67** (1), 158–168.

Leclercq, D.J.J. & Bohineust, X. 2002 Investigation and modelling of the wall pressure field beneath a turbulent boundary layer at low and medium frequencies. *J. Sound Vib.* **257** (3), 477–501.

Lighthill, M.J. 1952 On sound generated aerodynamically I. General theory. *Proc. of the Royal Society of London* **A 211**, 564–587.

Lund, T.S., Wu, X. & Squires, K.D. 1998 Generation of turbulent inflow data for spatially-developing boundary layer simulations. *J. Comput. Phys.* **140**, 233–258.

Mathew, J., Lechner, R., Foysi, H., Sesterhenn, J. & Friedrich, R. 2003 An explicit filtering method for large eddy simulation of compressible flows. *Phys. Fluids* **15** (8), 2279–2289.

Meecham, W.C. 1965 Surface and volume sound from boundary layers. *J. Acoust. Soc. Am.* **37**, 516–522.

Panton, R.L. & Robert, G. 1994 The wavenumber-phase velocity representation for the turbulent wall-pressure spectrum. *ASME Journal of Fluids Engineering* **116**, 477–483.

Phillips, O.M. 1956 On the aerodynamic surface sound from a plane turbulent boundary layer. *Proc. of the Royal Society of London* **234**, 327–335.

Powell, A. 1960 Aerodynamic noise and the plane boundary. *J. Acoust. Soc. Am.* **32** (8), 982–990.

Robinet, J.-C., Dussauge, J.-P. & Casalis, G. 2001 Wall effect on the convective-absolute boundary for the compressible shear layer. *Theoret. Comput. Fluid Dynamics* **15**, 143–163.

Schewe, G. 1983 On the structure and resolution of wall-pressure fluctuations associated with turbulent boundary-layer flow. *J. Fluid Mech.* **134**, 311–328.

Sevik, M.M. 1986 Topic in hydroacoustics. In *IUTAM Symp. on Aero- and Hydro-acoustics*, pp. 285–308. Lyon, France: Springer-Verlag.

Shariff, K. & Wang, M. 2005 A numerical experiment to determine whether surface shear-stress fluctuations are true sound source. *Phys. Fluids* **17** (107105).

Skudrzyk, F.J. & Haddle, G.P. 1960 Noise production in a turbulent boundary layer by smooth and rough surfaces. *J. Acoust. Soc. Am.* **32** (1), 19–34.

Smith, M.G. & Morfey, C.L. 2006 Directivity and sound power radiated by a source under a boundary layer. *AIAA Journal* **44** (11), 2630–2635.

Spalart, P.R. 1988 Direct simulation of a turbulent boundary layer up to $\mathrm{Re}_\theta = 1410$. *J. Fluid Mech.* **187**, 61–98.

Suzuki, T. & Lele, S.K. 2003 Green's functions for a source in a boundary layer: direct waves, channelled waves and diffracted waves. *J. Fluid Mech.* **447**, 129–173.

Tam, C.K.W. 1975 Intensity, spectrum, and directivity of turbulent boundary layer noise. *J. Acoust. Soc. Am.* **57** (1), 25–34.

Tam, C.K.W. & Dong, Z. 1996 Radiation and outflow boundary conditions for direct computation of acoustic and flow disturbances in a nonuniform mean flow. *J. Comput. Acous.* **4** (2), 175–201.

Tomkins, C.D. & Adrian, R.J. 2003 Spanwise structure and scale growth in turbulent boundary layers. *J. Fluid Mech.* **490**, 37–74.

Viazzo, S., Dejoan, A. & Schiestel, R. 2001 Spectral features of the wall-pressure fluctua-

tions in turbulent wall flows with and without perturbations using LES. *Int. J. Heat and Fluid Flow* **22**, 39–52.

Wang, M., Lele, S.K. & Moin, P. 1996 Sound radiation during local laminar berakdown in a low-Mach-number boundary layer. *J. Fluid Mech.* **319**, 197–218.

Willmarth, W.W. 1975 Pressure fluctuations beneath turbulent boundary layers. *Ann. Rev. Fluid Mech.* **7**, 13–38.

Willmarth, W.W. & Woolridge, C.E. 1962 Measurements of the fluctuating pressure at the wall beneath a thick turbulent boundary layer. *J. Fluid Mech.* **14**, 187–210.

Wills, J.A.B. 1970 Measurements of the wave-number/phase velocity spectrum of wall pressure beneath a turbulent boundary layer. *J. Fluid Mech.* **45**, 65–90.

Yang, Q. & Wang, M. 2009 Computational study of roughness-induced boundary-layer noise. *AIAA Journal* **47** (10), 2417–2429.